Université Libre de Bruxelles
Faculté des Sciences
Département de Physique

Investigating the impact of β stabilisation in JET hybrid plasmas through non-linear gyrokinetic simulations

Mémoire présenté en vue de l'obtention
du diplôme de master en sciences physique

Auteur:
Christopher Gerekos
Promoteur :
Dr. Sara Moradi

Année académique 2015-2016

Abstract

In this work we shall study the characteristics of core microinstabilities in a hybrid plasma from recent JET experiments with ITER-like wall (selected from ref. [8]) using non-linear global gyrokinetic simulations with the *GYRO* code [5]. Previous linear analysis has showed that in these high-β regimes, significant difference exists in the critical value of β for the onset of kinetic ballooning modes (KBMs) ; β_{crit} was found to be significantly higher in global than in local simulations [37]. These findings are important for future experiments at JET tokamak because of a possible rise of the upper power limit for regimes showing a lack of plasma confinement degradation [8], which is limited by destabilisation of KBMs at sufficiently high β.

Global simulations in the non-linear picture turned out to be much more demanding in time and computational power than what was foreseen for this thesis. Local analysis, however, has shown that the plasma does indeed seem to undergo an ITG-KBM transition in the non-linear case, and the behaviour observed was similar to that of the linear study [37]. These encouraging results mandate a follow-up study with global simulations.

Contents

Chapter 1

Introduction

To harness the power of nuclear fusion for civilian energy generation has been a major goal of physics since the '60s, notably through with the work of the scientists of the Kurchatov Institute, Novosibrinsk, U.S.S.R., who built the world's first successful tokamaks in 1968, although theoretical research on fusion dates back to the end of the Second World War [9]. Fusion power promises a durable, clean, safe, and fuel-efficient way to generate electricity for humanity's energy needs. Indeed, a 1 GW fusion-based power plant would only need about 250 kg of deuterium-tritium fuel per year, while a coal-fired plant consumes as much as 2.7 millions tons of coal a year to produce that same amount of energy [26]. The main by-product of a deuterium-tritium reactor is ^{4}He, an inert gas, making fusion a carbon-free energy source. Moreover, unlike fission-based plants, it would produce next to zero radioactive waste and presents no reactor meltdown mechanism. Additionally, fusion power could also bring disruptive changes to the field of space propulsion (see *e.g.* [50][17]) due to its very high energy density yield.

To this day the tokamak remains the most technologically mature way to achieve controlled fusion [40]. With a plasma volume of 100 m^3, the largest tokamak currently in operation is the *Joint European Torus* (JET), in the Culham Science Centre, U.K. [48], and is the most prominent precursor to the *International Thermonuclear Experimental Reactor* (ITER), currently in construction in Cadarache, France. The tokamak of ITER will have a plasma volume of about 2000 m^3 and a nominal ignited fusion power of 1.5 GW [40]. While ITER will not be an economical reactor *per se*, it is poised to become the most decisive step towards this goal so far. Most tokamaks operated today are able to generate fusion energy for short periods of time (a few seconds to a few tens of seconds [40]), but none so far has been able to achieve *ignition*, which is a state where the fusion is self-sustaining [13], that is, where the fusing plasma generates enough heat by itself and does not depend on external heating mechanisms to maintain useful energy generation. Based on current understanding of tokamak physics, ITER is predicted with great confidence to ignite [40].

A fusion process involves the merging of two atomic nuclei into a heavier nucleus (with some

possible leftovers such as neutrons) through strong interaction, one of the four fundamental interactions found in nature. In general, provided that the nuclei involved are lighter than ^{56}Fe (the nucleus with the highest binding energy per nucleon) the process will be exothermic [30]. An example of such a process is deuterium-tritium (D-T) fusion, which is often considered for fusion power plants for its large cross-section and other engineering-related reasons [49][25] :

$$^2\mathrm{H} + {}^3\mathrm{H} \rightarrow \left({}^4\mathrm{He} + 3.5\ \mathrm{MeV}\right) + \left(\mathrm{n} + 14.1\ \mathrm{MeV}\right). \tag{1.1}$$

To initiate a fusion process, the main obstacle to overcome is the electrostatic repulsion of the positively-charged nuclei. While the nuclei will indeed repel each other at larger distances, the short-range strong force will overcome the long-range electrostatic force once they are close enough. The electrostatic interaction can thus be thought as a potential barrier, and is usually called the *Coloumb barrier*. This barrier is typically very large, about 100 keV [49] for D-T reactions, and the reactants will need a considerable kinetic energy to surpass it. These kind of kinetic energies can be only be reached in plasmas with temperatures around 10 keV[(i)], that is, of several hundreds millions of Kelvins, and the main practical issue faced by the fusion community to this day is to find an efficient way to confine such a hot plasma.

A striking example of controlled fusion reactors found in nature are stars, which achieve confinement through the gravitational pull of their own mass (we speak of *gravitational confinement*), but there is obviously no way to reproduce this method on Earth in the foreseeable future due to the huge masses involved. A more practical method is *magnetic confinement*, where, as the name suggest, the plasma is confined via magnetic fields. Tokamaks operate along this paradigm, and are currently the most advanced and best understood designs [40], but other classes of devices exist, notably stellarators and field-reversed configurations. The last great class of methods is *inertial confinement*, which has been investigated in many ways, also with promising results (see *e.g.* [24]).

One of the most important problems in tokamak research is the study of instabilities, which are ominous in fusing plasmas. A better understanding of these processes would lead, broadly speaking, to better confinement. In 2015, a linear investigation of plasma microinstabilities was performed by Moradi *et al.* [37] through local and global gyrokinetic simulations using the state-of-the-art gyrokinetic code GYRO [5] and profiles coming from JET runs n° 84545 and 84792. It was discovered that, in local simulations, an ITG-KBM transition occurs as the plasma pressure is increased while global simulations showed, on the contrary, a suppression of ITGs at high plasma pressures, making them only marginally unstable (we will thoroughly explain the meaning of these technical terms later on.). These encouraging results in the global picture must now be confirmed with a non-linear study. This will be the focus of this work, which will make use of the same code and experimental profiles.

This document is structured as follows. The large second chapter is a review of the main concepts related to magnetically-confined plasmas (such as tokamak components, confinement

[(i)] The reason why the temperature needed is less than 100 keV simply resides in the fact the particles of the plasma have a Maxwellian distribution of speeds.

modes, and alternative technologies), the mathematical theory behind statistical description of plasmas and flux theory, and a rather comprehensive description of the main instabilities we are interested in. Chapter 3 will briefly outline the characteristics of GYRO, the programme we are using for this analysis. After having recalled the results from the linear study, the results of our non-linear study will be presented in chapter 4. Chapter 5 is dedicated to concluding remarks. Finally, more details about the characteristics of the JET run analysed (profiles and time traces) are given in Appendix A, while the simulation input files are given in Appendix B for reproducibility.

Chapter 2

Aspects of magnetically-confined fusion plasmas

This section can be thought as a broad introduction to magnetic confinement and fusion plasmas. We will first explore the physics of tokamaks and introduce a certain number of definitions and concepts about them. We shall then move on to the subject of plasma description, where we will outline the main steps towards the gyrokinetic theory, the most widely-used description for fusion plasmas. A short overview of plasma transport will then be given. Finally, the problem of plasma instabilities, which are at the core of this thesis, will be aborded.

Plasmas typically encountered in fusion reactors are fully-ionised and globally neutral [3]. Their temperature will usually be around 100 to 200 millions Kelvins and their density is about 1 mg/m^3 [48], which largely allows for a purely classical (non-quantum and non-relativistic) treatment. Moreover they will typically be placed within a magnetic field $\mathbf{B}(\mathbf{x}, t)$ and electric field $\mathbf{E}(\mathbf{x}, t)$.

2.1 Tokamak basics

As discussed in the introduction, one of the ways to confine a plasma is through magnetic fields, a technique known as *magnetic confinement*. Let us thus consider a particle with charge q and mass m in a constant and uniform magnetic field $\mathbf{B}(\mathbf{x}, t) = B\mathbf{u}_z$ (if the magnetic field isn't originally aligned with the z-axis, we can always rotate our system of coordinates accordingly). Using basic electrodynamic theory, it is possible to show, in the non-relativistic limit that charged particle will undergo a helical motion around a fixed axis, parallel to the magnetic field lines (see *e.g.* [33]) :

$$\begin{cases} x(t) = x_0 + \hat{\rho}_L \sin(\hat{\Omega}t + \iota), \\ y(t) = y_0 + \hat{\rho}_L \cos(\hat{\Omega}t + \iota), \\ z(t) = z_0 + \hat{v}_\parallel t, \end{cases} \tag{2.1}$$

where

$$\hat{\Omega} = \frac{|q|B}{m} \tag{2.2}$$

is the gyration frequency, and

$$\hat{\rho}_L = \frac{\hat{v}_\perp}{\hat{\Omega}} = \frac{\hat{v}_\perp m}{|q|B} \tag{2.3}$$

is the gyration radius, often known as the *Larmor radius*. $\hat{v}_\parallel$ and $\hat{v}_\perp$ respectively refer to the projections of the velocity of the particle on an axe parallel and perpendicular to the magnetic field ($\hat{v}_\parallel$ being in this case constant). Lastly, x_0, y_0, z_0, and ι are constants of motion.

Since these particles follow such constrained paths around the field lines, one can see that a straightforward way to confine a plasma would be by having field lines close on themselves in a circular way. This can be obtained by placing the plasma in a toroidal chamber with coils around the poloidal section of the torus. This kind of device is known as a *tokamak*. Other types of magnetic configurations exist, such as stellarators and field-reversed configurations, which will briefly be discussed in section 2.1.4.

The previous discussion assumed that the magnetic field was uniform, a situation which cannot be reached in toroidal configuration, where the toroidal component of the magnetic field will decrease as $B_t \propto \frac{1}{R}$ [49]. Making the assumption that the rate of change of the magnetic field is small, *i.e.* by considering $\mathbf{B}(\mathbf{x}) = \mathbf{B}_0 + \mathbf{x} \cdot \nabla B + \mathcal{O}(\nabla B)^2$ with $\frac{\mathbf{x} \cdot \nabla B}{B_0} \ll 1$, it can be shown that, in the first-order approximation, this gradient in the magnetic field will lead to a drift of the guiding centres in a direction perpendicular at a constant speed given by (see *e.g.* [33])

$$\mathbf{v}_{\nabla B} = \frac{\hat{v}_\perp \hat{\rho}_L}{2} \frac{\mathbf{B}_0 \times \nabla B}{B_0^2} \tag{2.4}$$

To compensate for this the ∇B drift in a tokamak, one can twist the magnetic field around the poloidal section. Since the particles will follow the field lines as they go inwards and outwards, they will experience drifts in opposite direction at different points of the chamber, and the ∇B drift will be cancelled on average.

Another class of guiding-centre drifts are those caused by a force acting on the particle. Again, using basic electrodynamics, one can show that a charged particle placed in an magnetic field $\mathbf{B}$ and subject to a force $\mathbf{F}$ (both considered homogeneous and constant for the sake of simplicity) will undergo a drift given by $\mathbf{v}_F = \frac{1}{q} \frac{\mathbf{F} \times \mathbf{B}}{B^2}$ (see *e.g.* [33]). In particular, if that force is commonplace electrostatic interaction, we find the expression for the so-called $\mathbf{E} \times \mathbf{B}$ *drift*

$$\mathbf{v}_{E \times B} = \frac{\mathbf{E} \times \mathbf{B}}{B^2}, \tag{2.5}$$

which plays an important role in plasma instabilities, as we'll see in sec. 2.4.

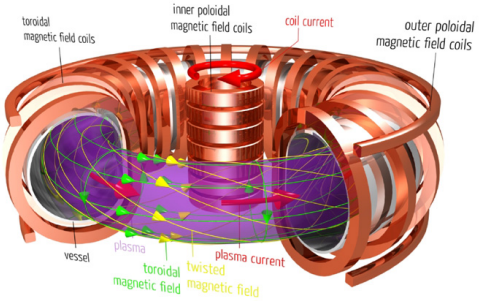

Figure 2.1 – Schematic of a simplified tokamak, showing the position of the different types of coils and their effect on the magnetic field. [51]

2.1.1 Main components of a tokamak

In the previous subsection we have outline the theoretical basis of the magnetic field in a tokamak. We will now look at the different aspects of a real-life tokamak.

Coils

The magnetic field in a tokamak is produced by two sets of coils, the toroidal coils, which are wrapped in multiple copies around the torus, and the poloidal coils, which circle around its inner and outer portions. As the name suggest, toroidal coils generate the toroidal component of the magnetic field, while the poloidal coils generate the poloidal twisting we mentioned. The two sets of coils can easily been seen on fig. 2.1.

Chamber

The chamber of the tokamak contains the hot plasma properly said. An appreciable part of it is covered by plasma-facing tiles which have stringent thermic properties, which is know as the *first wall*. High-Z metals such as Tungsten often make good plasma-facing materials but other elements such as Beryllium and Carbon have been investigated [2]. The release of impurities by the plasma-facing materials pose great problems in the way to ignition and is an active topic of research in the fusion community. We will however not concern ourselves with it in this thesis.

Instead of having a circular poloidal section, real-life tokamaks often display a D-shaped section, which allows to reduce the difference of magnetic field strength on each side of the chamber for a same plasma volume, hereby minimising the stress on the structure [49].

The dominant physics occurring in different parts of the tokamak can roughly be divided in four zones, as shown in fig. 2.2. The zone I, containing the so-called *core plasma* is where temperature and pressure will be the highest and consequently, where most fusion reactions will happen. Within zone I, these quantities reach their peak value near the magnetic axis [49]. In zone II, the *plasma edge*, a sharp decrease of temperature and pressure is observed [40]. The

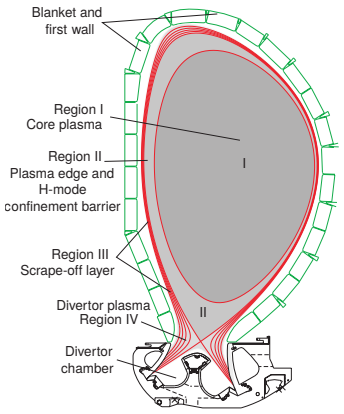

Figure 2.2 – The poloidal cross-section of ITER shows the typical D shape used on most tokamaks. Additionally, the name of the different plasma zones are indicated. [40]

plasma edge ends at the *separatrix*, which is an imaginary boundary that separates the field lines closing on themselves and those that close on the walls. Zone III is known as the *scrape-off* layer, and extends from the separatrix to the wall edge [13]. The magnetic field is generally designed in such a way that most particles crossing the separatrix, and thus finding themselves in the scrape-off layer, will be redirected into the zone IV. In this last zone, the *divertor region*, these particles will be flushed out of the system [13].

Divertor

The divertor is a component usually found at the bottom end of the poloidal section of the torus, as it can be see in the case of ITER in fig. 2.2. Its main role is to control the level of impurities the plasma, mostly through collisions [40]. These impurities can be fusion ashes (^{4}He in the case of D-T operations) or plasma-facing material sputtered from the chamber. The divertor of a tokamak is also used to address the issue of power dispersion, that is, to reduce the heat flux in regions III and IV of the plasma so that erosion of plasma-facing materials (and thus their lifetime) is kept acceptable [40]. Because of these roles, the design of the divertor will have a critical impact on the performance of the reactor, and as such, modelling its behaviour is also an active topic of research for the fusion community [49], but once again falls outside the scope of this thesis.

Heating mechanisms

A fusion plasma will have to be self-sustaining, *i.e.* be able to generate its own heat, in order for a reactor to be economical. For a D-T reactor, this indigenous heating will come from the kinetic energy of the ^{4}He particles (often called α-particles) released after every fusion reaction which will then thermalise. Before reaching a point where this indigenous heating is sufficient,

however, external mechanisms are needed to raise the plasma temperature. It is estimated that heating powers between 80 and 30 MW per GW of thermonuclear power at ignition are needed [49]. A typical tokamak run will involve several heating methods used consecutively. The initial heating is often done through *ohmic heating*, where a current is run through the plasma and will deposit energy in it through ohmic losses. From there, the most commonly-used methods to heat the plasma up to ignition are *RF heating*, where energy is transferred through the plasma via radiowaves and *neutral beam injectors* (NBI), which instil high-kinetic energy neutral atoms into the plasma, which will then ionise and raise the plasma temperature by momentum transfer [49].

2.1.2 Equilibrium concepts and definitions

The conditions for equilibrium in a tokamak plasma constitute the basis for the analysis of stability and transport. Additionally, there are several quantities commonly used in the literature to describe a tokamak plasma, all based on its equilibrium behaviour, which we are about to define.

The most basic aspect of tokamak equilibrium is the balance between plasma pressure and magnetic confinement force (mechanical equilibrium), which translates into the condition that

$$\mathbf{j} \times \mathbf{B} = \nabla p, \tag{2.6}$$

although other aspects pertaining to the shape of the plasma exist [49]. We will assume that the tokamak is a revolution volume, *i.e.* that it has toroidal symmetry, which is true to a very good approximation in real-life devices [12]. From the mechanical equilibrium condition, we have immediately that $\mathbf{B} \cdot \nabla p = \mathbf{j} \cdot \nabla p = 0$, from what we can infer that there are no pressure differences along the magnetic fields lines and that the current lines lie on surfaces of constant magnetic field [49].

Grad-Shafranov equation

The Grad-Shafranov equation is a second-order partial differential equation describing the shape of the so-called *magnetic flux function* $\psi(r, \theta)$, through two arbitrary functions $p(\psi)$ and $f(\psi)$. This is the equation solved by GYRO [6] and other fusion simulation programmes to find the flux surfaces.

From $\nabla \cdot \mathbf{B} = 0$ in cylindrical coordinates, we find that

$$\frac{1}{r}\frac{\partial}{\partial r}(rB_r) + \frac{\partial B_z}{\partial z} = 0, \tag{2.7}$$

where B_r and B_z are the components of the magnetic field in the radial and z-direction respectively (no term with derivatives with repsect to ϕ is present because of the axysimmetry condition). Consequently, we can define a « flux function » ψ such that [49]

$$B_r \equiv \frac{-1}{r}\frac{\partial \psi}{\partial z}, \qquad B_z \equiv \frac{1}{r}\frac{\partial \psi}{\partial r}. \tag{2.8}$$

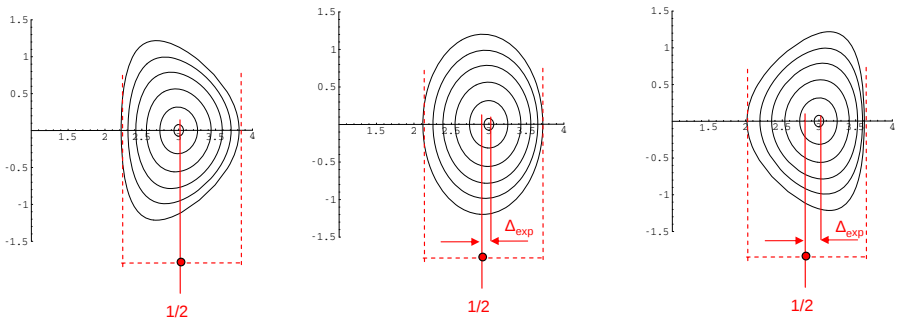

Figure 2.3 – Cross-section of flux surfaces for different plasma triangularities. The complete surfaces can be visualised by revolving these cross-sections around the poloidal axis. On the horizontal axis, which represents r/R, 1/2 is the middle of the tokamak and Δ_{exp} is the Shafranov shift. [21]

This function ϕ thus has the following property

$$\mathbf{B} \cdot \nabla\psi = 0, \tag{2.9}$$

from which we can see that magnetic field lines lie on surfaces of constant ψ, hence their name. Additionally, one can similarly show that a « current flux function » f must exist ; it is defined as

$$j_r \equiv \frac{-1}{r}\frac{\partial f}{\partial z}, \qquad j_z = \frac{1}{r}\frac{\partial f}{\partial r}, \tag{2.10}$$

and can be shown to be a function of ψ : $f = f(\psi)$ [49].

The equation ruling their shape, the Grad-Shafranov equation reads, [49]

$$r\frac{\partial}{\partial r}\frac{1}{r}\frac{\partial\psi}{\partial r} + \frac{\partial^2\psi}{\partial z^2} = -\mu_0 r^2 p'(\psi) - \mu_0^2 f(\psi) f'(\psi), \tag{2.11}$$

where $p(\psi)$ is the pressure and $f(\psi)$ the current flux function defined at eq. (2.10). A derivation of this equation can be found, *e.g.* in refs. [49] or [21]. The solutions of this equation are typically nested torus-like surfaces [49], as it can be seen in fig. 2.3.

A consequence of this equation is the fact that the centres of the flux surfaces do not coincide with the magnetic axis for most plasma geometries. This property is known as the *Shafranov shift* [21][49] and can be physically understood as a consequence to the fact that the internal pressure will tend to push the plasma outwards. An important quantity related to the Shafranov shit $\Delta(r)$ is the α_{MHD} parameter, which is defined through

$$\frac{\partial\Delta}{\partial r} = \alpha_{MHD}. \tag{2.12}$$

Characterisation of this shift is important for the study of MHD (magnetohydrodynamic) instabilities, altough this falls outside the scope of this thesis.

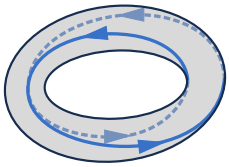

Figure 2.4 – A field line with a q factor of 2 in a tokamak. [49]

β parameter

The β parameter is defined as the ratio of the average plasma pressure p to the average magnetic pressure $B^2/2\mu_0$ [49] :

$$\beta \equiv \frac{2\mu_0 p}{B^2}. \tag{2.13}$$

A necessary condition to have confinement is that the magnetic pressure is inferior to the plasma pressure, which translates as $\beta < 1$. Broadly speaking, a high β value is desirable for a magnetically-confined fusion devices, since it would mean that lower magnetic field strengths are needed in order to achieve the same plasma pressure. This is however difficult to apply because high β values begets important MHD instabilities [23]. The highest β value ever reached by a tokamak was $\beta = 0.4$, a record set by the Small Tight Aspect Ratio Tokamak (START) at the Culham Science Centre, U.K. [23]. If we define a « normalised » beta $\beta_N \equiv \beta a B I^{-1}$, which cancels out the effects of the dimensions of the tokamak, it can be shown that above a certain threshold (known as the *Troyon limit*), the MHD instabilities of the plasma take over and a brutal loss of confinement ensues [22][32]. Troyon initially calculated this value to be $\beta_N \gtrsim 0.028$ [45], although experimental values rather seem to indicate $\beta_N \gtrsim 0.035$ [22].

The β parameter of a is often used as a sort of « figure of merit » for fusion devices, and does not apply solely to tokamaks (it is, for instance, also used to characterise theta- and z-pinch devices [38]). Other types of β parameters can also be defined, for instance, by only considering one component of the magnetic field (poloidal or toroidal) or by considering one species of particles only (ions or electrons).

Safety factor

The safety factor q is a scalar associated with each magnetic field line which is defined as follows. If a field line needs to accumulate an amount $\Delta\phi$ of toroidal angle variation in order to close on itself, that field line will have a safety factor [49]

$$q \equiv \frac{\Delta\phi}{2\pi}. \tag{2.14}$$

In other words, the safety factor expresses the number of « laps » a field line has to do around the toroidal direction in order to come back to the point it started. A field line with $q = 2$ has been represented on fig. 2.4. Its name comes from the fact that a high safety factor will generally lead to greater stability [49].

If we decompose the magnetic field into its poloidal and toroidal components, $\mathbf{B} = B_p\mathbf{u}_p + B_\phi\mathbf{u}_\phi$, the safety factor can be calculated via the following formula [49]

$$q = \frac{1}{2\pi}\oint \frac{1}{R}\frac{B_\phi}{B_p}ds \tag{2.15}$$

Since q is obviously the same for all magnetic lines on the same magnetic surface, the safety factor is a flux function : $q = q(\psi)$.

When considering the variations of q along the radial axis (we speak of q *profiles*), one finds that the function obtained usually acquires a U-shape, with the minimum close to the magnetic axis [49][32].

2.1.3 Confinement modes and scaling laws

Confinement time

Let W be the total energy present in the fusing plasma and P_L the power continuously being lost by it, *e.g.* through neutrons, radiative cooling, loss of plasma mass or momentum. We can define a quantity known as the *confinement time* τ_E, which will be the ratio between the two :

$$\tau_E \equiv \frac{W}{P_L}. \tag{2.16}$$

If the confinement time is sufficiently high, the tokamak will be able to reach a point where the indigenous heating will be sufficient to offset all losses. This is known as *ignition*. Using simple energetic arguments and basic nuclear physics considerations, it can be shown that a condition for ignition in a D-T reactor is that $n\tau_E > \frac{12}{\langle\sigma v\rangle}\frac{T}{\mathcal{E}_\alpha}$ [49], where T is the plasma temperature (here taken to be constant for simplicity), $n = n_D + n_T$ the total ion density, $\langle\sigma v\rangle$ is a quantity related to the reaction rate[(i)] and $\mathcal{E}_\alpha$ is the kinetic energy of α-particles at creation.

Experimentally, the confinement time will often be given as a power law of several physical parameters such as the tokamak dimensions. These formulae, often referred to as *scaling laws*, will depend on the confinement mode used. Fig. 2.5 illustrates the application of such a scaling law from several existing devices to ITER.

Tokamak modes

Different tokamak regimes have been discovered, each with its own scaling law, some much more advantageous for fusion power generation than other. We will now quickly review the most common modes.

Ohmic and L-Mode. The *ohmic mode* refers to plasma behaviour in purely ohmically-heated devices. Albeit an extremely inefficient way to reach ignition, ohmic heating can provide useful

[(i)] More precisely, the quantity $\langle\sigma v\rangle$ is a statistical average of the reaction cross-section and the mean particle velocity, up to a normalisation, so that the reaction rate $\mathcal{R} = n_D n_T \langle\sigma v\rangle$. The exact form can be found in [49].

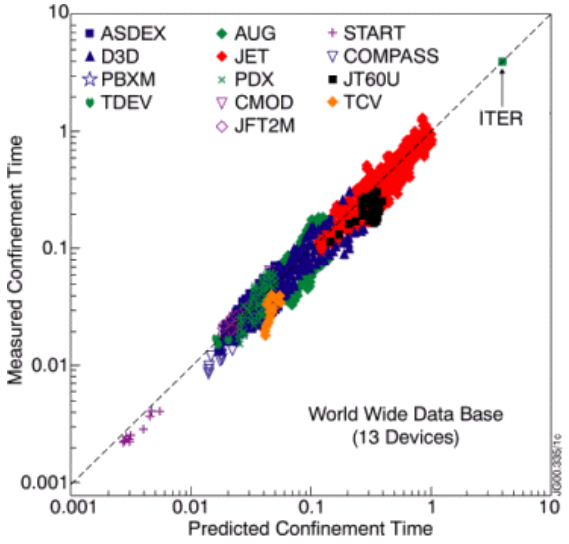

Figure 2.5 – Logarithmic plot of the theoretical and measured confinement time for a wide ensemble devices, which illustrates the concept of scaling law. [10]

insights on confinement in general. In the linear ohmic regime, that is when the plasma density is below a saturation value, the confinement time is given by the so-called *neo-Alcator scaling* [12][19]:

$$\tau_E(s) = 0.07 n_e (10^{20}\ m^{-3}) q \kappa^{0.5} R(m)^2 a(m), \tag{2.17}$$

where q is the safety factor defined at eq. (2.15) at the plasma surface, κ the plasma elongation ratio (the cross-section height divided by its width [13]), R and a the major and minor radius of the tokamak, respectively.

If additional heating mechanisms, such as NBI or RF heating (briefly discussed in sec. 2.1.1) are used, the temperature and plasma energy will increase, but not as much as one would have expected from ohmic scalings such as (2.17) [12]. This mode with deteriorated confinement time is known as the *low confinement mode* or *L-mode*. A fusion device based on L-mode operations would have to be inconveniently large to attain ignition [12].

H-mode. When enough NBI heating is supplied to the plasma, however, an sudden transition to a mode with much better confinement properties was discovered [12][49]. This *high-confinement mode* or *H-mode* was first observed in the Axially Symmetric Divertor Experiment (ASDEX) tokamak, at the Max-Planck-Gesellshaft für Plasmaphysik, Germany [12][47]. This mode is envisioned as one of the primary operating mode for ITER for a number of reasons, including its robustness and reproducibility, its good confinement even at high densities, the fact that it requires no special current profile to be maintained, and because its flat density profile allows for reduced impurity accumulation at the tokamak centre [12][2]. The most prominent feature of the H-mode is the spontaneous formation of a transport barrier at the plasma edge,

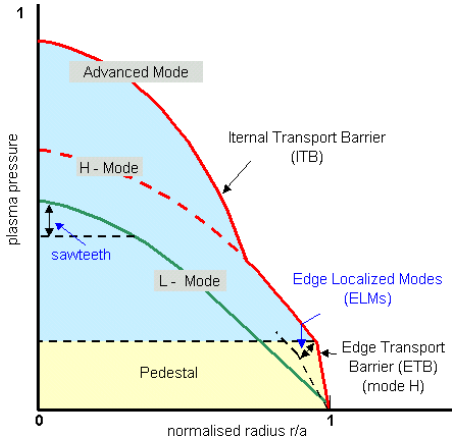

Figure 2.6 – Schematic representation of the plasma density profiles for the main tokamak confinement modes identified so far. [10]

which is known as the *edge pedestal*, and is associated with instabilities known as *edge-localised modes* (ELMs) [49], which consist of rapid oscillations that provoke pulsed plasma losses. While ELMs degrade energy confinement by about 10 to 20%, they do help flushing impurities and fusion ashes out of the reactor [2][12]. The differences between L- and H- mode confinement is qualitatively shown on fig. 2.6.

Several scaling laws have been devised for H-mode runs, which may differ due to the database used or whether they include ELMs. A widely-used one is the *IPB98(y,2)* scaling, which is expressed by [12]

$$\tau_{E,\mathrm{th}}^{\mathrm{ELMy}} = 0.0562 I^{0.93} B^{0.15} P^{-0.69} n^{0.41} M^{0.19} R^{1.97} \epsilon^{0.58} \kappa^{0.78}, \tag{2.18}$$

where I is the plasma current, B the toroidal magnetic field at the major radius R, P the power losses, n the average density, M the average ion mass, and ϵ the inverse aspect ratio of the tokamak.

One can also use normalised scaling laws to better compare the discharges between them. In particular, the so-called $H98$ *factor* is defined as

$$H98y = \frac{\tau_E}{\tau_{\mathrm{IPB98}}}, \tag{2.19}$$

where τ_E is the observed confinement time and τ_{IPB98} is the IPB98(y,2) scaling defined at eq. (2.18).

Hybrid mode. During ITER operations, ELMy H-mode confinement is expected to yield a very high fusion gain (about $Q = 10$) during short periods of time (approx. 400 s) making use of large plasma currents ($I_p = 15$ MA) while the so-called *steady-state* scenario would have a lower yield (about $Q = 5$) for much longer period of time (approx. 5000 s) using lower currents ($I_p = 9$ MA) [20]. The *hybrid scenario* or *improved H-mode* aims at having both a high yield

during extended periods of time, and that, with even lower plasma currents than for the H-mode (a yield $Q = 10$ for 3000 s at $I_p = 12$ MA is sought) [20][36]. Hybrid discharges also have other interesting properties regarding fusion power generation such as higher β_N and better control over some type of instabilities [20] .

Recent experiments at JET and other tokamaks have shown that such a confinement mode is reached by using very specific heating profiles, such a current overshoot over a classical ramp-up approach [36]. Hybrid discharges are typically characterised by a low magnetic shear ($q \approx 1$) at the centre of the plasma [36].

In this thesis, the discharges investigated, JET runs n° 84545 and 84792, are of this type [37].

2.1.4 Alternatives to tokamaks

While tokamaks are the most mature way to achieve sustained power generation, they are subject to a number of issues such as instabilities, as we'll see in greater detail in sec. 2.4, or the fact that they need to be made rather large to achieve satisfying confinement times. Other types of fusion devices have been experimented with, each with their own advantages and drawbacks with respect to tokamaks. We will succinctly have a look at two of them, the *stellarator* and the *field-reversed configuration*.

Stellarators

The idea behind the stellarator is to « twist » the plasma surface in the poloidal direction in order to naturally suppress some instabilities and drifts otherwise inherent to the tokamak [29]. For instance, both the ∇B and the $\mathbf{E} \times \mathbf{B}$ drifts described at the beginning of this section are automatically cancelled thanks to the poloidal rotation induced on the plasma [29]. Moreover, they can operate continuously while tokamaks can only operate in pulsed mode once the external heating mechanisms are taken away [34]. The chamber of a stellarator is no longer axisymmetric but possesses n-fold symmetry instead, which can on the other hand induce other problems such as increased particle loss [29]. A schematic representation of such a device is shown on fig. 2.7.

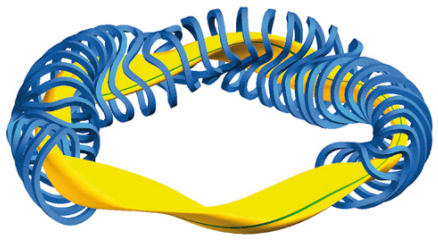

Figure 2.7 – Schematic representation of the plasma surface (yellow) and coils (blue) of the W7X stellarator, showing the characteristic plasma shape in these kind of devices, which unlike tokamaks is no longer a revolution volume. [34]

It is not yet known if stellarators will effectively deliver an easier way to achieve controlled fusion power, and more experimental investigation is needed. With a major plasma radius of 5.5 m, the Wendelstein 7-X (W7X) device, currently in construction at the Max-Planck-Gesellshaft für Plasmaphysik, Germany, will be the largest stellarator operated to this day, and is expected to deliver important insights in that regard [34].

Field-reversed configuration

Field-reversed configuration (FRC) devices are a class of plasma pinch confinement systems [43], that is, when an electrical current is sent into the plasma to generate a magnetic field that will compress it. FRCs are compact toroidal apparati with both open and closed field lines, which have the advantage of being intrinsically very high-β devices and possessing a « natural » divertor [43]. They are attractive as fusion reactors mostly because of their much smaller size when compared to tokamaks or stellarators [43], and as a consequence, are preferred for applications such as future spacecraft propulsion or energy generation systems [41][16]. The basic magnetic field configuration of a FRC can be seen on fig. 2.8.

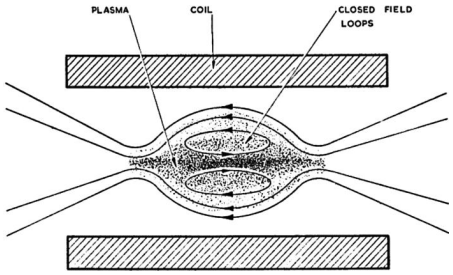

Figure 2.8 – Early conceptual design of a field-reversed configuration device. [43]

Research on FRCs has historically been more scattered and the current state of knowledge is much less advanced than for tokamaks [43]. Issues pertaining to stability, operation theory and pulse longevity are still largely unsolved [43].

2.2 Description of plasmas

In this section we will present the main aspects of the theory of statistical description of plasmas, with a particular focus on the so-called *gyrokinetic theory*, which is one of the most successful in the field of fusion physics.

Let us consider classical plasma made of N_e electrons and N_i ions, for a total number of particles $N = N_e + N_i$. We will refer to each species with a subscript α. At a microscopic level, such a system will be described by an Hamiltonian given by [3]

$$H(\mathbf{q}_1, \mathbf{p}_1, ..., \mathbf{q}_N, \mathbf{p}_N, t) = \sum_{\alpha=e,i} \sum_{j=1}^{N_\alpha} H_\alpha(\mathbf{q}_j, \mathbf{p}_j; t), \tag{2.20}$$

with

$$H_\alpha(\mathbf{p},\mathbf{q};t) = \frac{1}{2m_\alpha}\left|\mathbf{p} - \frac{q_\alpha}{c}\mathbf{A}(\mathbf{q};t)\right|^2 + q_\alpha\phi(\mathbf{q};t), \tag{2.21}$$

where $\mathbf{q}$ and $\mathbf{p}$ are the canonical positions and impulsion the subscript, $\mathbf{A}(\mathbf{q},t)$ and $\phi(\mathbf{q},t)$ respectively refer to the vector potential and the electrostatic potential associated with the magnetic and electric fields mentioned above, and finally m_α and q_α are respectively the mass and charge of each species of particle. The equations of motion of this system will be given by

$$\begin{cases} \dot{\mathbf{q}}_j = [\mathbf{q}_j, H] = \frac{\partial H}{\partial \mathbf{p}_j} \\ \dot{\mathbf{p}}_j = [\mathbf{p}_j, H] = -\frac{\partial H}{\partial \mathbf{q}_j} \end{cases}, \tag{2.22}$$

where the Poisson bracket of two variables A and B is defined as [18]

$$[A,B] = \sum_{n=1}^{N}\left(\frac{\partial A}{\partial \mathbf{q}_n}\cdot\frac{\partial B}{\partial \mathbf{p}_n} - \frac{\partial A}{\partial \mathbf{p}_n}\cdot\frac{\partial A}{\partial \mathbf{q}_n}\right) \tag{2.23}$$

For systems of macroscopic size, the number of differential equations contained in the set (2.22) is of the same order of magnitude as Avogadro's constant $N_A \approx 10^{23}$, a fact which naturally rules out any hope for direct solving. The exact motion of all particles of the system may furthermore not be needed for most purposes. Statistical methods must thus be devised, which, coupled with approximations and assumptions on the system, will reduce the complexity of the problem down to one solvable with current computational power.

2.2.1 Fully-kinetic description

Instead of solving for the motion of individual particles, we will rather try to describe the evolution of the *density of probability* $\mathcal{F}(\mathbf{q},\mathbf{p};t)$ that a particle is at a position $\mathbf{q}$ and has an impulsion $\mathbf{p} = m\dot{\mathbf{q}}$ at instant t. The equation describing this evolution is the *Fokker-Planck equation*, which can be shown to take the form [18] :

$$\frac{\partial \mathcal{F}_\alpha}{\partial t} + \frac{\mathbf{p}}{m_\alpha}\cdot\frac{\partial \mathcal{F}_\alpha}{\partial \mathbf{q}} + \mathbf{F}_\alpha\cdot\frac{\partial \mathcal{F}_\alpha}{\partial \mathbf{p}} = \mathcal{K}_\alpha, \tag{2.24}$$

where, as previously, we adjoined a subscript α to discriminate between the two species of particles. In the left-hand side of (2.24), $\mathbf{F}_\alpha(\mathbf{q},\mathbf{p};t)$ represents the force exerted on a particle, which can be of any origin (gravitational, electromagnetic, *etc.*), while the term $\mathcal{K}_\alpha$ on the right-hand side represents the collision operator, which has to be modelled after a theory. For example, in the simplest case of a colloidal particle in suspension in a fluid, that operator will be given by $\frac{\partial}{\partial \mathbf{p}}\cdot\left(\frac{\zeta_\alpha}{m_\alpha}\mathbf{p}\mathcal{F}_\alpha\right) + \zeta_\alpha k_B T_\alpha \frac{\partial^2 \mathcal{F}_\alpha}{\partial \mathbf{p}^2}$, where ζ_α is the friction coefficient and T_α the temperature[(ii)] [18]. More complex collision operators can be used, such as the one implemented by GYRO (see the GYRO technical guide [6] for a full description). The derivation of the Fokker-Planck equation

[(ii)] The attentive reader will have remarked that T bears an subscript α as well. Indeed, because the system is not necessarily at equilibrium, the temperature of electrons T_e and of ions T_i isn't necessarily equal.

from Liouville's equation, which establishes the conservation of probability in the 6-dimensional phase space, can be found, *e.g.* in [18].

The Fokker-Planck equation can be more elegantly written in terms of Poisson anticommutators :

$$\frac{\partial \mathcal{F}_\alpha}{\partial t} - [H_\alpha, \mathcal{F}_\alpha] = \mathcal{K}_\alpha. \tag{2.25}$$

When changes in the distribution through collisions can be neglected, which is the case is very high temperature plasma [3], we may set $\mathcal{K}_\alpha = 0$ in eq. (2.25), for all species α. The equation obtained, a collisionless Fokker-Planck equation, is known as the *Vlasov equation* :

$$\boxed{\frac{\partial \mathcal{F}_\alpha}{\partial t} - [H_\alpha, \mathcal{F}_\alpha] = 0}. \tag{2.26}$$

Additionally, if we chose Lorentz' force for $\mathbf{F}_\alpha$, we get the so-called Vlasov-Maxwell equation :

$$\frac{\partial \mathcal{F}_\alpha}{\partial t} + \frac{\mathbf{p}}{m_\alpha} \cdot \frac{\partial \mathcal{F}_\alpha}{\partial \mathbf{q}} + q_\alpha \left[\mathbf{E}(\mathbf{q}, t) + \frac{\mathbf{p}}{c m_\alpha} \times \mathbf{B}(\mathbf{q}, t) \right] \cdot \frac{\partial \mathcal{F}_\alpha}{\partial \mathbf{p}} = 0. \tag{2.27}$$

This equation is still too complex to be solved. Indeed, the electrical and magnetic fields have to be solved self-consistently from Maxwell's equation and depend strongly on $\mathcal{F}_\alpha$, and we're still left with a highly-nonlinear problem. More mathematical groundwork is thus needed in order to obtain a workable equation. The next subsections will outline the steps towards the *gyrokinetic equation*, which is the one used by most fusion research codes, including GYRO. The main idea behind gyrokinetics is to take advantage of properties of fusion plasmas (such as, for instance, the fact that the Larmor radii of the plasma particles are much smaller than the rate of change of the magnetic field), and « average over » the fast gyromotion of the particles to treat only charged rings « quasiparticles » [27][39]. This discussion follows rather closely the one given at ref. [3] and the reader is invited to consult it for more details.

2.2.2 Guiding-centre variables

The first step towards the gyrokinetic equation is to decompose the electromagnetic fields and their potential as an average and fluctuating part [3]

$$\begin{aligned} \mathbf{E}(\mathbf{x}; t) &= \mathbf{E}_0(\mathbf{x}) + \delta\mathbf{E}(\mathbf{x}; t), \qquad & \mathbf{B}(\mathbf{x}; t) &= \mathbf{B}_0(\mathbf{x}) + \delta\mathbf{B}(\mathbf{x}; t), \\ \phi(\mathbf{x}; t) &= \phi_0(\mathbf{x}) + \delta\phi(\mathbf{x}; t), \qquad & \mathbf{A}(\mathbf{x}; t) &= \mathbf{A}_0(\mathbf{x}; t) + \delta\mathbf{A}(\mathbf{x}; t). \end{aligned} \tag{2.28}$$

This implies that the Hamiltonian admits such a decomposition as well :

$$H_\alpha(\mathbf{q}, \mathbf{p}; t) = H_{0,\alpha}(\mathbf{q}, \mathbf{p}) + \delta H_\alpha(\mathbf{q}, \mathbf{p}; t). \tag{2.29}$$

We will now define the so-called *guiding-centre variables*, which will allow us to considerably simplify the problem with the help of some assumptions. The transformations that link the new (non-canonical) variables $(\mathbf{X}, \mathbf{Y})$ to the original ones $(\mathbf{q}, \mathbf{p})$ are known as *pseudo-canonical transformation* and leave the Vlasov equation (2.25) invariant.

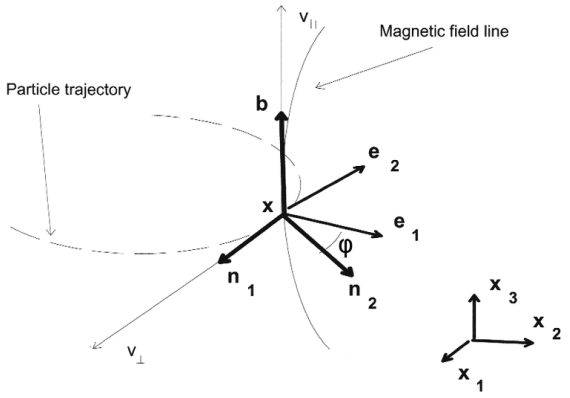

Figure 2.9 – The fixed local reference frame $(\mathbf{e}_1, \mathbf{e}_2, \mathbf{e}_3 \equiv \hat{\mathbf{b}})$ and the moving local reference frame $(\mathbf{n}_1, \mathbf{n}_2, \mathbf{n}_3 \equiv \hat{\mathbf{b}})$, plotted along the absolute reference frame $(\mathbf{x}_1, \mathbf{x}_2, \mathbf{x}_3)$. The gyrophase $\hat{\varphi}$ of the particle is the angle formed between $\mathbf{e}_1$ and $\mathbf{n}_2$. [3]

The first transformation is the switch from $\mathbf{p}$ to a quantity $\hat{\mathbf{v}}$ related to the particle velocity :

$$\mathbf{q} = \mathbf{q}, \qquad \hat{\mathbf{v}} = \frac{1}{m_\alpha}\left[\mathbf{p} - \frac{q_\alpha}{v}\mathbf{A}_0(\mathbf{q})\right]. \tag{2.30}$$

Next, we define a *local fixed reference frame*, $(\mathbf{e}_1, \mathbf{e}_2, \mathbf{e}_3)$ depending on the orientation of the (average) magnetic field as follows : $\mathbf{e}_1(\mathbf{x})$ is directed along the principal normal of the magnetic field line, $\mathbf{e}_2(\mathbf{x})$, along its binormal, while $\mathbf{e}_3(\mathbf{x}) \equiv \hat{\mathbf{b}}(\mathbf{x})$ is parallel to that magnetic field line. Suppose the following decomposition for $\hat{\mathbf{v}}$: $\hat{\mathbf{v}} = \hat{v}_\parallel \hat{\mathbf{b}}(\mathbf{q}) + \hat{\mathbf{v}}_\perp$. We also define a *local moving reference frame* $(\mathbf{n}_1, \mathbf{n}_2, \mathbf{n}_3)$ as follows : $\mathbf{n}_1$ is parallel to $\hat{\mathbf{v}}_\perp$, $\mathbf{n}_2 \equiv \hat{\mathbf{b}} \times \mathbf{n}_1$, and $\mathbf{n}_3 \equiv \mathbf{e}_3$. The *gyrophase* $\hat{\varphi}$ of a particle will then be defined as the angle between $\mathbf{e}_1$ and $\mathbf{n}_2$. All the objects we just defined were reported on fig. 2.9 for better clarity. We can now define the second pseudo-canonical transformation, connecting the previous set of variables $(\mathbf{q}, \hat{\mathbf{v}})$ to the new one $(\mathbf{q}, \hat{v}_\parallel, \hat{v}_\perp, \hat{\varphi})$:

$$\mathbf{q} = \mathbf{q}, \qquad \hat{\mathbf{v}} = \hat{v}_\parallel \hat{\mathbf{b}}(\mathbf{q}) + \hat{v}_\perp \mathbf{n}_1(\mathbf{q}, \hat{\varphi}) \tag{2.31}$$

When calculating the equations of motion of particles from these variables, an important problem is the fact that they depend on the gyrophase $\hat{\varphi}$. The last pseudo-canonical transformation, based on the *Kruskal-Littlejohn theorem* [3] aims to weed out this dependence. This transformation, which takes the coordinates of a particle, $\hat{z}^m = \{\mathbf{q}, \hat{v}_\parallel, \hat{v}_\perp, \hat{\varphi}\}$, abbreviated $\hat{z}^m$ $(m = 1, ..., 6)$, to a new set of coordinates $z^m = \{\mathbf{Y}, v_\parallel, v_\perp, \varphi\}$, is such that all the Lie brackets of these new variables are independent from the gyrophase,

$$\left[z^k, z^m\right] = \sum_{km} \left(z^1, ..., z^5\right), \qquad k, m = 1, ..., 6, \tag{2.32}$$

and that the unperturbed Hamiltonian is independent of the gyrophase

$$H_{0,\alpha} = H_{0,\alpha}\left(z^1, ..., z^5\right). \tag{2.33}$$

This transformation only makes sense if the Larmor radii of the particles $\hat{\rho}_{L,\alpha}$, defined at eq. (2.3), are much smaller than the « smallest characteristic macroscopic length of the system » L_M, which can here be taken to be $L_M = |\nabla \ln B|^{-1}$ [3], that is,

$$\hat{\epsilon} \equiv \frac{\hat{\rho}_{L,\alpha}}{L_M} \ll 1, \tag{2.34}$$

an assumption known as the *drift approximation*.

The new set of variables z^m are called the *guiding centre variables*, with the vector $\mathbf{Y}$ representing the spatial coordinates of the gyrocentre. The relationship between the particle coordinates and the guiding centre coordinates are, to the first relevant orders in $\hat{\epsilon}$:

$$\mathbf{q} = \mathbf{Y} + \frac{v_\perp}{\Omega_\alpha(\mathbf{Y})}\mathbf{n}_2(\mathbf{Y},\varphi) + \mathcal{O}\left(\hat{\epsilon}^2\right), \tag{2.35}$$

$$\mathbf{v} = v_\parallel \hat{\mathbf{b}}(\mathbf{Y}) + v_\perp \mathbf{n}_1(\mathbf{Y},\varphi), \tag{2.36}$$

where

$$v_\parallel = \hat{v}_\parallel + \mathcal{O}\left(\hat{\epsilon}\right), \qquad v_\perp = \hat{v}_\perp + \mathcal{O}\left(\hat{\epsilon}\right), \qquad \varphi = \hat{\varphi} + \mathcal{O}\left(\hat{\epsilon}\right). \tag{2.37}$$

The equations of motion will now be given by

$$\dot{z}^k = \left[z^k, H_\alpha\right] = \sum_{j=1}^{6} \left[z^k, z^j\right] \frac{\partial H_\alpha}{\partial z^j}. \tag{2.38}$$

We can see that, while the Poisson brackets of the z^m coordinates are independent of the gyrophase, the equations of motion themselves still show such a dependence. This is known as *finite Larmor radius* (FLR) effects. Through more assumptions we will be able to have an equation that does not depend on the φ, the gyrokinetic equation.

2.2.3 Gyrokinetic description

Because the Vlasov equation is here a stochastic equation, we can decompose the distribution function (which is in this case a random, fluctuating function) into an average and fluctuating part :

$$\mathcal{F}_\alpha = F_\alpha + \delta f_\alpha, \tag{2.39}$$

with $F_\alpha = \langle \mathcal{F}_\alpha \rangle$ and $\langle \delta f_\alpha \rangle = 0$, where the $\langle A \rangle$ represents the ensemble-average of A.

Vlasov's equation (2.27) thus reads

$$\left(\partial_t + \dot{z}^m \frac{\partial}{\partial z^m}\right)\left(F_\alpha + \delta f_\alpha\right) = 0, \tag{2.40}$$

where the $z^m = (\mathbf{Y}, v_\parallel, v_\perp, \phi)$ are the guiding-centre coordinates introduced from eqs. (2.32) to (2.38). By performing an ensemble-average on this equation, we find an equation for the distribution average F_α :

$$\partial_t F_\alpha + \langle \dot{z}^m \rangle \frac{\partial}{\partial z^m} F_\alpha + \left\langle \dot{z}^m \frac{\partial}{\partial z^m} \delta f_\alpha \right\rangle = 0, \tag{2.41}$$

and, substracting this equation from (2.40), we find an equation for the fluctuation δf_α :

$$\partial_t \delta f_\alpha + \left(\dot{z}^m - \langle \dot{z}^m \rangle\right) \frac{\partial}{\partial z^m} F_\alpha - \left\langle \dot{z}^m \frac{\partial}{\partial z^m} \delta f_\alpha \right\rangle + \dot{z}^m \frac{\partial}{\partial z^m} \delta f_\alpha = 0. \tag{2.42}$$

As noted before, when calculating the equations of motion 2.38 in order to find the $\dot{z}^m$ quantities explicitly, we find that there's still a dependence on the gyrophase φ. Consequently we find that the two equations (2.41) and (2.42) we just derived will depend on φ as well. More gyroaveraging is thus required to completely eliminate dependence in gyrophase. To this end, we propose to separate each phase-space function $A(\varphi)$ into

$$A(\varphi) = \overline{A} + \tilde{A}(\varphi), \tag{2.43}$$

with the *gyro-averaged* part $\overline{A}$ obeying $\overline{A} = (2\pi)^{-1} \int_0^{2\pi} d\varphi A(\varphi)$. In order for this modification of notation to produce meaningful simplification of eq. 2.42, we must make several more assumptions on the system, which are all largely-verified for fusion plasma [3][27]. The assumptions, which broadly define the range of application of gyrokinetics are the following.

We first demand that the *thermal drift parameter* ϵ is small [3][27] :

$$\epsilon \equiv \frac{\rho_{L,\alpha}}{L_M} \ll 1, \tag{2.44}$$

where $\rho_{L,\alpha}$ is a quantity known as the *thermal Larmor radius* of species α, which has the same form as the Larmor radius given at eq. (2.3) but with the thermal velocity $V_{T,\alpha} = (2T_{0,\alpha}/m_\alpha)^{1/2}$ instead of $\hat{v}_\perp$, and L_M is again the shortest macroscopic length scale of the system. We also require that the condition of *weak turbulence* is met [3][27] :

$$\lambda \equiv \frac{\delta f_\alpha}{F_\alpha} \sim \frac{q_\alpha \delta\phi}{T_{0,\alpha}} \ll 1. \tag{2.45}$$

We finally suppose that parallel gradients of fluctuating quantities are very small [3][27], an assumption known as the *gyrokinetic ordering*,

$$\mu \equiv \frac{k_\parallel}{k_\perp} \sim \frac{\omega}{\Omega_\alpha} \ll 1. \tag{2.46}$$

Very often, $\epsilon \sim \lambda \sim \mu$ will be assumed as well [3].

Explicit results for the shearless slab geometry

Armed with these drastic simplifications we will be able to produce a workable equation. We now propose to display the final gyrokinetic equation for a very simple case, known as the *shearless slab geometry*. This model involves a stationary, homogeneous magnetic field and an electric field with a zero average, *i.e.* $\mathbf{E}_0(\mathbf{x}) = \phi_0(\mathbf{x}) = 0$ as well as $\delta\mathbf{A}(\mathbf{x};t) = \delta\mathbf{B}(\mathbf{x};t) = 0$ in eqs. (2.28). The magnetic field can thus be noted as $\mathbf{B} = B_0\ \hat{\mathbf{b}}$.

Using the formalism explained above, we introduce two quantities. The first is the *electrostatic drift velocity* $\delta\mathbf{V}^E \equiv \frac{c}{B_0}(\hat{\mathbf{b}} \times \nabla\overline{\delta_\phi})$, and the second is the *parallel acceleration* (as in, parallel to

the magnetic field) $\delta a_\alpha = \frac{-q_\alpha}{m_\alpha}(\hat{\mathbf{b}} \cdot \nabla \overline{\delta\phi})$. From there it can be shown [3] the Vlasov equation (2.41) for the distribution average F_α can be written as

$$\boxed{\partial_t F_\alpha = -\nabla \cdot \left(\hat{\mathbf{b}} v_\parallel F_\alpha\right) - \nabla \cdot \left\langle \delta \mathbf{V}^E \delta f_\alpha \right\rangle - \frac{\partial}{\partial v_\parallel} \left\langle \delta a_\alpha \delta f_\alpha \right\rangle}, \tag{2.47}$$

while the one (2.42) for the fluctuation δf_α as

$$\boxed{\partial_t \delta f_\alpha + v_\parallel \hat{\mathbf{b}} \cdot \nabla \delta f_\alpha + \mathcal{Q}\left(\delta \mathbf{V}^E \cdot \nabla \delta f_\alpha\right) = -\delta \mathbf{V}^E \cdot \nabla F_\alpha - \delta a_\alpha \frac{\partial F_\alpha}{\partial v_\parallel}}, \tag{2.48}$$

where the operator $\mathcal{Q}$ beign defined as $\mathcal{Q}(\delta A_1 \delta A2...) \equiv \delta A_1 \delta A2... - \langle \delta A_1 \delta A2... \rangle$.

Equations (2.47) and (2.48) are the gyrokinetic equations for the shearless slab geometry and can be used to compute the total distribution functions $\mathcal{F}_\alpha$ of each plasma species α. Finally, the system can be rendered self-consistent if we include Poisson's equation for the electrostatic potential in terms of the particle distribution:

$$\boxed{\nabla^2 \delta\phi = -4\pi \sum_{\alpha=e,i} q_\alpha \int d\mathbf{V} \delta f_\alpha}. \tag{2.49}$$

This shearless slab model is quite simple, but may nevertheless be useful when studying phenomena where the effects of toroidal curvature can be neglected, such as some microinstabilities [49]. More complete and realistic models exist, obviously, but they will generate more cumbersome equations. The reader is invited to consult ref. [3] for a more comprehensive review.

2.3 Fluxes and transport theory

Transport theory concerns itself with the exchange of some physical quantity within fluids by its constituants, and henceforth seeks to determine *particle fluxes* and their relationship with the thermodynamic forces causing them. Particle transport is strongly related to the study of microinstabilities, as they are an important source of transport (and more specifically, *anomalous transport* [49], that is transport due to stochastic fluctuations, as we'll see at the end of this section). Will thus devote this section to define these particles fluxes in the gyrokinetic approximation. As for the previous section, ref. [3] is followed rather closely.

Using notation from sec. 2.2.3, the *particle number density* for the species α is defined as [3]

$$n_\alpha(\mathbf{x}; t) = \int d\mathbf{v} \int d\mathbf{Y} \delta\left[\mathbf{x} - \mathbf{q}(\mathbf{Y})\right] \left[F_\alpha(\mathbf{Y}, \mathbf{v}; t) + \delta f_\alpha(\mathbf{Y}, \mathbf{v}; t)\right], \tag{2.50}$$

which very naturally decomposes into an ensemble-averaged and a fluctuating part :

$$n_\alpha(\mathbf{x}; t) = n_{\alpha,0}(\mathbf{x}; t) + \delta n_\alpha(\mathbf{x}; t). \tag{2.51}$$

For the average part, we can replace the position of the particle $\mathbf{q}$ with the position of the guiding centre $\mathbf{Y}$ with an error comparable to ϵ [defined at eq. (2.44)], whereas, to maitain order

of approximation coherence within our formula, we take into account finite Larmor radius effects for the fluctuating part. We thus obtain [3]

$$n_{\alpha,0}(\mathbf{x};t) \simeq \int d\mathbf{v} \int d\mathbf{Y} \delta(\mathbf{x}-\mathbf{Y}) F_\alpha(\mathbf{Y},\mathbf{v};t), \tag{2.52}$$

$$\delta n_\alpha(\mathbf{x};t) \simeq \int d\mathbf{v} \int d\mathbf{Y} \delta \left[\mathbf{x}-\mathbf{Y}-\frac{v_\perp}{\Omega_\alpha}\mathbf{n}_2(\varphi)\right] \delta f_\alpha(\mathbf{Y},\mathbf{v};t), \tag{2.53}$$

where we made use of eq. (2.35) to write the second relation.

The number of particles for a given species is clearly a conserved quantity[(iii)] and we postulate that the average particle number density obeys a conservation law :

$$\partial_t n_{\alpha,0}(\mathbf{x};t) = -\nabla \cdot \mathbf{\Gamma}_\alpha(\mathbf{x};t) \tag{2.54}$$

where $\mathbf{\Gamma}_\alpha(\mathbf{x};t)$ is the *particle flux* for the species α.

For the shearless slab geometry, we have an explicit formula for $\partial_t F_\alpha$, which is given by (2.47). Inserting it into the time-derivative of eq. (2.52), performing the integration over the $\mathbf{Y}$ along with some algebraic operations to « factor out » the derivatives, we find [3]

$$\partial_t n_{\alpha,0}(\mathbf{x};t) = -\nabla \cdot \int d\mathbf{v} \left[v_\parallel \hat{\mathbf{b}} F_\alpha(\mathbf{x},\mathbf{v};t) - \left\langle \delta\mathbf{V}^E(\mathbf{x},v_\perp;t)\delta f_\alpha(\mathbf{x},\mathbf{v};t)\right\rangle\right]. \tag{2.55}$$

Comparing with eq. (2.54), we find the expressions for the components of the particle flux :

$$\Gamma_{\alpha,\parallel} = \int d\mathbf{v} v_\parallel F_\alpha(\mathbf{x},\mathbf{v};t), \tag{2.56}$$

$$\mathbf{\Gamma}_{\alpha,\perp} = \frac{c}{B}\int d\mathbf{v} \left\langle \delta V^E(\mathbf{x};t)\delta f_\alpha(\mathbf{x},v;t)\right\rangle. \tag{2.57}$$

Again, the expressions are only valid for the shearless slab geometry and would get more cumbersome when more realistic magnetic and electric fields were considered.

We can remark that the parallel flux does only depend on F_α and is thus purely deterministic, while this is not the case for the two perpendicular components of $\mathbf{\Gamma}_\alpha$, which indeed depends of the distribution fluctuations δf_α. The perpendicular fluxes is for this reason referred to as *anomalous* [3]. In general, when looking at transport in tokamaks, an arbitrary flux $\mathbf{J}$ may be decomposed as

$$\mathbf{J} = \mathbf{J}^{\mathrm{CL}} + \mathbf{J}^{\mathrm{NCL}} + \mathbf{J}^{\mathrm{AN}}, \tag{2.58}$$

where $\mathbf{J}^{\mathrm{CL}}$ represents the *classical flux*, that is, the contribution to the total flux determined by individual collision processes in a constant magnetic field, $\mathbf{J}^{\mathrm{NCL}}$ represents the *neoclassical flux*, which is the contribution determined again, by collision theory, but with the inclusion of magnetic curvature and inhomogeneity, while finally $\mathbf{J}^{\mathrm{AN}}$ regroups the ensemble-average effects due to stochastic fluctuations [3]. While neoclassical theory forms a standalone mathematical formalism, this is not yet the case for anomalous transport theory [3].

[(iii)] The losses due to nuclear reaction are vastly negligible with respect to the total number of plasma particles.

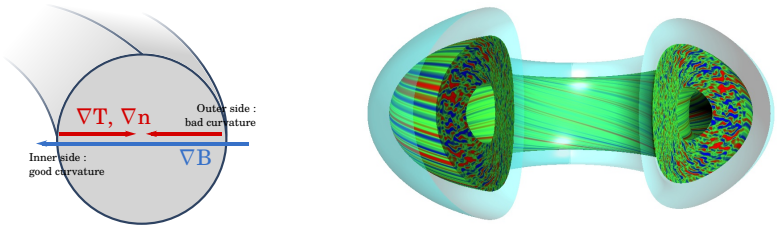

Figure 2.10 – Left : Poloidal cross-section of a tokamak showing how the relative orientations of magnetic and thermodynamic gradients define a « good » and a « bad » curvature region. Right : Electron density fluctuations within a tokamak plasma, as simulated with GYRO, exemplifying how curvature regions affect mode growth. [5]

2.4 Plasma instabilities

Understanding instabilities in plasmas constitute one of the most important issues faced by the fusion community today. Indeed, achieving stability in a reactor is a necessary condition for steady power generation. In this section, we will review the main type of instabilities that we are interested in.

Modes can be classified following their scale. We shall take the product $k_n\rho_{L,i}$ of the mode wavenumber and the ionic Larmor radius as our reference length. Large-scale isntabilities ($k_n\rho_{L,i} \ll 1$) such as *sawtooth crashes* or *neoclassical tearing modes* (NTMs) [22] are difficult to investigate with gyrokinetics since they affect length scales comparable to the tokamak size. Those are usually studied using MHD or neoclassical theory instead, putting them outside the scope of this thesis, but the interested reader will find more informations in refs. [3][12][22]. On the other hand, very small-scale instabilities ($k_n\rho_{L,i} \gg 1$) such as electron temperature gradient (ETG) modes or some trapped electron modes (TEMs) are so small that they do not generate significant anomalous particle transport[(iv)]. Note that such small-scale modes are mainly driven by electrons since their Larmor radius is much smaller than the ions'. The kind of instabilities in which we are mainly interested in happen on a scale $k_n\rho_{L,i} \lesssim 1$. As we'll see, those consist mostly of ion temperature gradient (ITG) modes and kinetic ballooning modes (KBMs), which we are about to describe in greater detail.

A useful concept to introduce for instability study pertains to tokamak curvature regions. We've seen in sec. 2.1 that plasma pressure and temperature were highest near the centre of the poloidal section tokamak while the magnetic field decreases as roughly $1/r$ from the centre of the tokamak itself. When plotting the gradients of these quantities, we obtain a situation schematically represented at fig. 2.10-left. As we will see, in the inner region, the magnetic field gradient and the pressure/temperature gradients have opposing directions, and instabilities are suppressed while on the outer region, these gradients are all aligned, leading to unstable mode growth.

[(iv)] In fact, this can depend on the device itself, its geometry and its fuelling mechanisms. For instance, TEMs in ASDEX plasmas can generate non-negligible transport [35].

2.4.1 Ion temperature gradient (ITG) mode

ITGs are a type of instability associated with ion temperature gradients and are mainly driven through a $\mathbf{E} \times \mathbf{B}$ drift on the bad tokamak side.

The physical process behind ITG formation can be explained as follows [4]. Since a hot ion has a greater velocity than a cold one, it will naturally drift faster, as it can be seen from eq. (2.4). If we place ourselves on the bad tokamak side, the temperature, pressure and magnetic gradients are all aligned, with the high-temperature plasma being « inside » the colder plasma as shown in fig. 2.11. The ion drift speed difference between these zones will then lead to ion density fluctuations, which will in turn generate localised electric fields. Because of those fields, ions will be subject to a $\mathbf{E} \times \mathbf{B}$ drift that will, in this case, tend to push the hot plasma pockets further outside and the cold plasma pockets inwards, accentuating the initial fluctuation. On the good side of the tokamak, however, where the temperature gradient is pointing in the opposite direction (but the magnetic field gradient still pointing in the same direction), the $\mathbf{E} \times \mathbf{B}$ drift suppresses it.

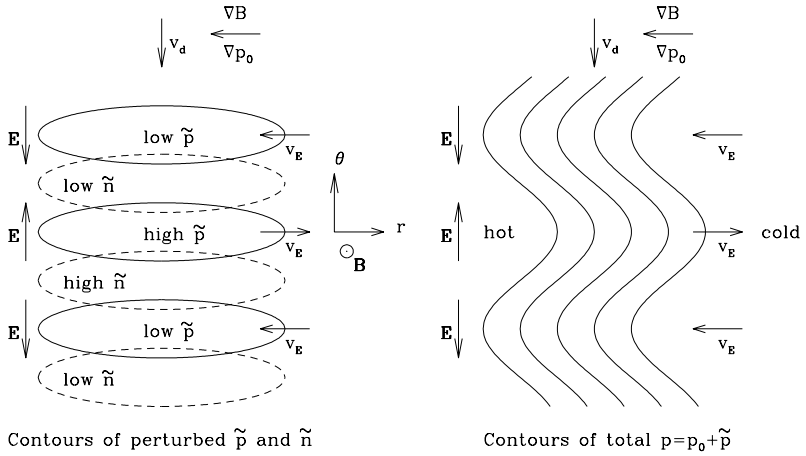

Figure 2.11 – Intuitive mechanism for the apparition of ITGs on the bad tokamak side. Quantities with a tilde represent fluctuations. [4]

Using the gyrokinetic description and neglecting FLR effects, it is possible to show the existence of a mode with a growth rate given by [4]

$$\omega = \frac{6\omega_d\zeta + 2\omega_d - \omega_*}{2\zeta} \pm \frac{\sqrt{(6\omega_d\zeta + 2\omega_d - \omega_*)^2 - 4\zeta\left[6\omega_d^2(1+\zeta) + 2\omega_d\omega_*(\eta_i - 2)\right]}}{2\zeta} \tag{2.59}$$

where

$$\eta_i \equiv \frac{L_{n,i}}{L_{T,i}} = \frac{\left(\frac{d\ln T_{0,i}}{dr}\right)}{\left(\frac{d\ln n_0}{dr}\right)} \tag{2.60}$$

is the ratio of the equilibrium density scale length to the equalibrium temperature scale length, $i\omega_* \equiv \frac{cT_{0,i}}{qB^2 n_0}\mathbf{B}\times\nabla n_0\cdot\nabla p_0$ and $i\omega_d \equiv \frac{cT_{i,0}}{qB^3}\mathbf{B}\times\nabla B\cdot\nabla p_0$ are respectively the so-called diamagnetic

and toroidal drift frequencies, and finally $\zeta \equiv \tau + b = T_{0,i}/T_{0,e} + k_\perp^2 \rho_i^2$ is a positive dimensionless parameter.

The η_i parameter is important in the determination of the mode behaviour, hence the name η_i *modes* seldom given to ITGs. By taking the limit $\eta_i \to \infty$, we can see that the mode frequency (2.59) reduces to :

$$\omega \approx \pm i \sqrt{\frac{2\omega_d \omega_* \eta_i}{\zeta}}. \tag{2.61}$$

Since $\omega_d \omega_* \eta_i$ must be positive for the frequency to be imaginary, we see from the definitions of ω_d and ω_* that ∇p_0 and ∇B must point in the same direction to have an unstable mode, *i.e.* we must be near the bad curvature region [4]. The mode described by eq. (2.61) is known as the toroidal ion temperature gradient mode, and corresponds to the mechanism we previously described[(v)].

2.4.2 Kinetic ballooning mode (KBM)

Kinetic ballooning modes are also a class of instabilities mainly driven by bad curvature effects. Their mechanism of formation is not as straightforward as for ITGs, but the main difference with those is that KBMs are triggered by magnetic fluctuations rather than temperature gradients and typically appear above a certain critical β [42]. In fact, « ballooning modes » appear in MHD theory alone (that is, when no kinetic effects are considered), and KMBs are usually defined as the instability obtained when incorporating kinetics effects into these purely-MHD ballooning modes [42]. Using *ideal* MHD theory (that is, MHD theory where resistive effects are neglected), it can be shown that the onset of ballooning modes is controlled by a parameter α (with onset requiring $\alpha \simeq 1$) with related to the magnetic pressure β as follows [42] :

$$\alpha = \frac{q^2 \beta_i}{\epsilon_n} \left[1 + \eta_i + (1 + \eta_e)/\tau\right], \tag{2.62}$$

where q is the safety factor, β_i the ionic β parameter, η_i the parameter defined at eq. 2.60, η_e its electronic analogue, and $\tau \equiv T_{0,i}/T_{0,e}$. The situation is different when kinetic effects are taken into account, but the α defined above remains a good indicator for onset to a factor of two [42].

Regarding growth rates, it can be shown [42] that when plotting them as a function of the plamsa pressure β, one obtains a function resembling that of fig. 2.12-left. ITGs are suppressed with increasing β while KBMs start to appear at some critical value, as explained above. One can see that there seen to be a « island of stability » around $\beta \approx 0.017$, but this region of zero growth actually disappears when kinetic effects are taken into account [42]. Note that a physical description such as the one we gave for ITGs is much more difficult to lay out. Additionally, an analytical solution for the growth rate is going to be extremely cumbersome to handle if one wants to account for most relevant effect [35].

[(v)] The $\pm$ in front of 2.61 simply shows that there are two different modes, and only the growing one will be of interest to us.

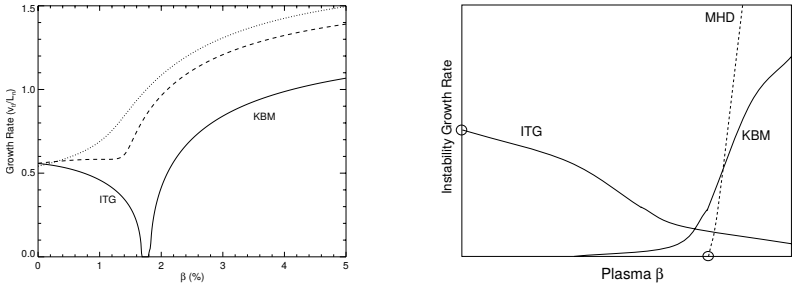

Figure 2.12 – Left : Schematic representation of the growth rate of the dominant mode in ideal MHD theory, broken down to ITG modes and ballooning modes, as a function of the plasma pressure β. Dashed lines show how the growth rate looks like with more complete theories. Right : Schematic representation of an ITG-KBM transition (the dashed lines indicated the pure-MHD ballooning mode). [42]

When experimentally investigating these instabilities through a β sweep, a ITG-KBM transition will usually look like fig. 2.12-right.

Chapter 3

Overview of GYRO

GYRO is an open-source computer programme developed by General Atomics since 1999 [7]. Described as a « nonlinear tokamak microturbulence package » by its authors [7], it solves the gyrokinetic equation along with the Maxwell equations to determine fluctuating plasma quantities, such as electrostatic fluctuations, and transport across flux surfaces. Indeed, the distribution function $f(\mathbf{x}, \mathbf{q}; t)$ depends on $\mathbf{E}(\mathbf{x}; t)$ and $\mathbf{B}(\mathbf{x}; t)$, which themselves depend on f, so these equations must be solved together. The task of GYRO is thus to solve this five-dimensional system of differential equations. As we saw in sec. 2.2.2 during the derivation of the gyrokinetik hypotheses, all electromagnetic fields were divided into an average and a fluctuating part. The average part is determined assuming equilibrium and using Maxwell's equations only (f is taken to be a Maxwellian distribution), which in this case results in $\mathbf{E}_0(\mathbf{x}) = 0$ since the plasma is quasi-neutral while $\mathbf{B}_0(\mathbf{x})$ is given by the externally-applied magnetic field. The initial conditions we use to solve these equation are plasma profiles, which can come, as in our study, from experimental runs.

GYRO solves the aforementioned equations in an iterative way, and the solutions for the distribution function $f(\mathbf{x}, \mathbf{q}; t)$ and fluctuating quantities of interest $\delta\phi(\mathbf{x}; t)$, $\delta\mathbf{A}(\mathbf{x}; t)$, *etc.* are available for each time-step (a more precise definition of this time-step will be given shortly). From there, other quantities of interest such as the fluxes can be computed (see *e.g.* eqs. 2.56 and 2.57 for particle flux).

In this short chapter, we will briefly review the main aspects of transport study with GYRO. We will start by outlining how are plasma profiles calculated from experimental data. We shall then move on to precising what are the different kind of boundary conditions that can be used. Finally, some more details on the simulation outputs we're interested in will be given.

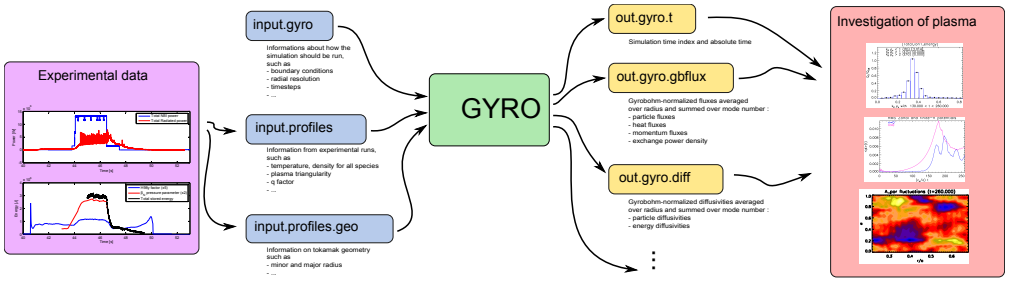

Figure 3.1 – Block diagram of the main files involved in the use of GYRO, how they are generated and how they are used.

3.1 Plasma profiles

Plasma profiles are equilibrium physical quantities such as temperature, pressure or q-factor presented as functions of radius. In our case, these profile come form actual JET runs. We will now quickly explain how these profiles are generated from raw experimental data.

During a plasma run, there will usually be a short time window during which the plasma is at a state close to equilibrium, usually lasting a few seconds depending on external factors such as heating mechanisms. Phases such as current ramp-up or decay obviously fall outside this category. Once this windows has been selected, 0.5 seconds-long subwindows are created, each 0.1 seconds appart (these subwindows are thus overlapping). For each of these, we compute the relative standard deviation of all quantities, $\sigma_{r,\lambda} \equiv \sigma_\lambda / \nu_\lambda$, where σ_λ and ν_λ are, respectively, the standard deviation and average of quantity λ over the 0.5s subwindow. After taking the average over all quantities λ, we select the windows which has the smallest result.

We can then assume that all parameters during this windows are approximately constant and reasonably close to the equilibrium value, and only the radial dependence remains.

3.2 Boundary conditions

To solve the gyrokinetic equations numerically one has to discretise the tokamak plasma. GYRO offers two types of boundary conditions, namely *local* or *global*.

A local simulation assumes *periodic boundary conditions* at the end of the radial domain. We are thus working in a so-called *flux-tube geometry*, that is, a restricted radial domain following a magnetic field line. The field line that is followed in particular is determined by the input q-profile and the selection of the radius at which the simulation is carried. The thickness of the tube can also be selected in GYRO simulations. Those kind of conditions are useful for local linear or restricted non-linear analyses but aren't compatible with profile variations. In practice, that means that these boundary conditions will stop yeilding accurate results whenever distant events in the tokamak will affect the simulation domain, a situation which typically occurs if the magnetic shear nears zero [35]. However, as we'll see, there are a number of issues with global

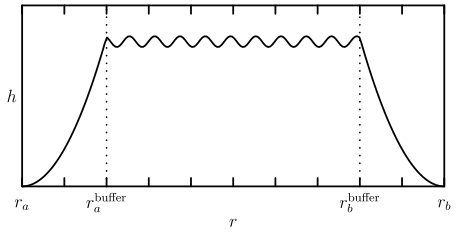

Figure 3.2 – Schematic representation of the « benign » Dirichelet condition used in global simulation with GYRO for a given field h. [6]

simulations, so it will be good practice to have local results to make a comparison.

Global simulations, on the other hand, use what the authors call « benign » Dirichlet condition. If one used pure Dirichelet condition, that is, if one imposes the fields take a zero value at the ends of the domain, experience shows that violent, unphysical oscillations will occur [6]. The workaround used by the authors was to demand the field undergo an exponential decay, as show in fig. 3.2. This, in turn, can lead to change in the equilibrium profile as the simulation evolves [6], which is unphysical as well. To counteract this, it is possible to add an artificial flux source (called « adaptative source » by the GYRO authors) that will mimick the effects or the surrounding plasma in an actual toroid. Correctly setting the magnitude of this source is a matter of ongoing discussion, and the extent to which the results coming out from such simulations can be trusted remains controversial [35].

3.3 Output quantities

Let us quickly review the different quantities that can be investigated with GYRO and how they are relevant to draw a complete picture of the behaviour of the plasma.

Fluxes. One of the quantities we are interested in are the particle fluxes $\Gamma_\alpha/\Gamma_{GB}$ and the heat fluxes $Q_{0,\alpha}/Q_{GB}$, where α stands for electrons or ions. Γ_{GB} and Q_{GB} are factor that normalise these quantities in a way known as *gyrobohm-normalisation* :

$$\Gamma_{GB} \equiv \bar{n}_e \bar{c}_s \left(\bar{\rho}_{s,\text{unit}}/a\right)^2 , \tag{3.1}$$

$$Q_{GB} \equiv \bar{n}_e \bar{c}_s \bar{T}_e \left(\bar{\rho}_{s,\text{unit}}/a\right)^2 . \tag{3.2}$$

A bar on a quantity indicates that it is taken at the reference radius. $\bar{n}_e$ represents the electron density at the reference radius, $\bar{T}_e$ the electron temperature, $\bar{c}_s = \sqrt{\bar{T}_e/m_D}$ the ion sound speed, and finally $\bar{\rho}_{s,\text{unit}} = \bar{c}_s m_D c/e\bar{B}_{s\text{unit}}$ the ion sound gyroradius. a is the minor radius of the tokamak.

Particle and heat fluxes are used to determine whether plasma has reached a quasi-steady state, which is the state we're interested in to study microinstabilities. A positive value indicates

an outward flux (away from the centre). Typically, fluxes will rapidly increase at the beginning of a run and will then stabilise to their quasi-equilibrium value, as we'll see in sec. 4.3.

Time is also normalised and is indicated as multiples of the $a/\bar{c}_s$ elementary time unit.

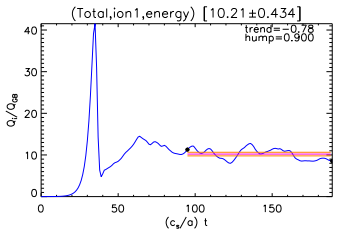

Figure 3.3 – Exemple of thermal flux evolution plot, showing the typical peak followed by a stabilisation.

Potential frequency response. Looking at the occurrence of electrostatic modes in a frequency versus toroidal mode number allows to discriminate between the different kind of modes that are present in the plasma. Indeed, ITGs, KBMs and TEMs have each a specific range of frequencies which is easy to identify in such a picture. For instance, a value of -0.2 is typical of ITGs. More details will be given in sec. 4.3.

Frequencies are indicated as multiples of $\bar{c}_s/a$ and mode numbers as multiples of $1/\bar{\rho}_s$. These plots are generated by selecting a relevant time window within the run in which the plasma has reached a quasi-steady state.

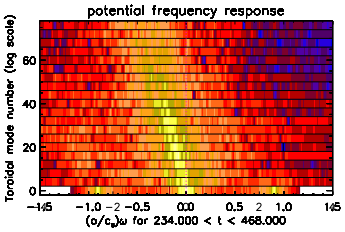

Figure 3.4 – Exemple of potential frequency response plot, showing the occurrence of modes in a frequency versus toroidal mode number fashion (a zero toroidal wavelength corresponds to the zonal flow).

Mode histogram. An important diagnostic tool for analysing plasmas is the distribution of thermal energy per electrostatic mode, classified with their normalised wavevector. As for the frequency response plot, each mode has a specific range of wavelength, and identifying which modes carry the most energy is useful to study the global behaviour of the plasma, as it will be done is sec. 4.3.

Thermal energy is normalised through Q_{GB} defined above at eq. (3.2). Wavelengths k_θ on the other hand are normalised through the ion sound gyroradius.

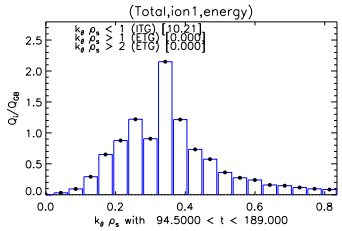

Figure 3.5 – Example of mode histogram, showing the distribution of ion thermal energy per mode.

Evolution of electrostatic modes. GYRO also allows to look at the time-evolution of the amplitude of electrostatic modes. These mode are divided into two categories : the $n = 0$ modes, which is known as the zonal flow, and $n > 0$ modes, which correspond to microinstabilities. Typically, the zonal flow will increase at the detriment of microinstabilities as we move forward in time, as we'll see in sec. 4.3.

Time is indicated as multiples of the $a/\bar{c}_s$ elementary time unit.

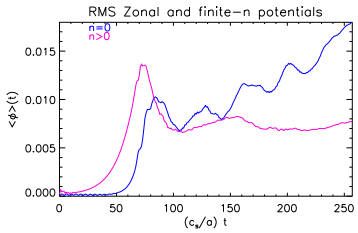

Figure 3.6 – Exemple of time-evolution plot for electrostatic modes, where the typical « shearing » of microinstabilities by the zonal flow over time is apparent.

Chapter 4

Non-linear investigation of core microinstabilities

In 2015, Moradi *et al.* performed a linear study of plasma instabilities through local and global GYRO simulations [37]. The authors performed a β-scan on three tokamak regions. Near the core region, it was discovered that, in local simulations, the plasma undergoes a ITG-KBM transition as β increases while global simulations showed a stabilisation of the plasma, with ITGs becoming only marginally unstable. These global results are very encouraging since they imply that β can be significantly increased in tokamaks without a massive increase in transport, allowing for better confinement without necessarily stronger magnetic fields. The picture obtained in the linear study (where only the largest mode is looked at) should now be confirmed non-linearly (where all modes are taken into account), which is the focus of this work, as mentioned in chapter 1.

After having introduced the theory behind tokamaks, gyrokinetics, transport and instabilities at chapter 2 and outlined how GYRO works at chapter 3, we will now enter the heart of the subject properly said, that is, our non-linear gyrokinetic study of plasma instabilities. We will first specify what experimental data we are working with, we will then recall the linear simulation results in greater detail, and eventually analyse our own results. Future perspectives are given at the end of the chapter.

4.1 Profiles, dataset and outline of the simulations

Experimental profiles for this study come form JET run n° 84545 which was part of the 2013-2014 JET experimental campaign [8]. Five β cases were investigated in this non-linear study :

- Zero beta, $\beta = 0$.
- Low beta, $\beta = 0.5\beta_{\text{exp}}$.

- Experimental beta, $\beta = \beta_{\text{exp}}$.
- Intermediate high beta, $\beta = 1.2\beta_{\text{exp}}$.
- High beta, $\beta = 1.5\beta_{\text{exp}}$.

β_{exp} represents the experimental value of the beta parameter, which is determined from the JET run itself. In GYRO the beta parameter of the simulation is tweaked by scaling β in all equations solved [6].

Of all these runs, only the first three have fully-converged, as we're about to see. However, despite the fact that the two higher beta cases are still within the convergence phase and have not reached a quasi-steady state, we believe they already contain valuable enough information to draw some conclusions.

More details about the discharge we are investigating (time traces and profiles) can be found in Appendix A, while the GYRO parameters of these simulations in particular are made available in Appendix B for reproducibility.

4.2 Main results of the linear analysis

In the study from Moradi *et al.*, two JET hyrbid discharges from [8] were analysed, namely runs 84545 and 84792, using both local and global gyrokinetic simulations. The authors looked at the evolution of the real and imaginary frequencies of the most unstable mode when β is increased, and that, in the following tokamak radial versions : $\rho = 0.3$, 0.45, and 0.65. After having analysed the results for experimental Shafranov shift and magnetic shear, additional analyses were performed on these two parameters to single out the reasons for the observed behaviour.

We will only comment the results for the $\rho = 0.45$ zone since it is that region that we investigated non-linearly.

4.2.1 Global-local comparison

The results of the « base » simulation, where all plasma parameters except β were kept to their experimental level, are shown in fig. 4.1. Both discharges showed similar behaviour, so only discharge n° 84545 is displayed.

We can see that the growth rate of the most unstable mode diminishes as β increases from 0 to its experimental value (0.01). The normalised frequency of this mode lies at -0.3, which is typical of an ITG mode [35]. In that range of β, local and global simulations depict a very similar picture.

As β is increases beyond its experimental value, local simulations show that the growth rate of the largest mode increases again while its frequency suddenly settles around -1. This is an ITG-KBM transition [35], and is associated with greater matter transport and thus lesser confinement quality.

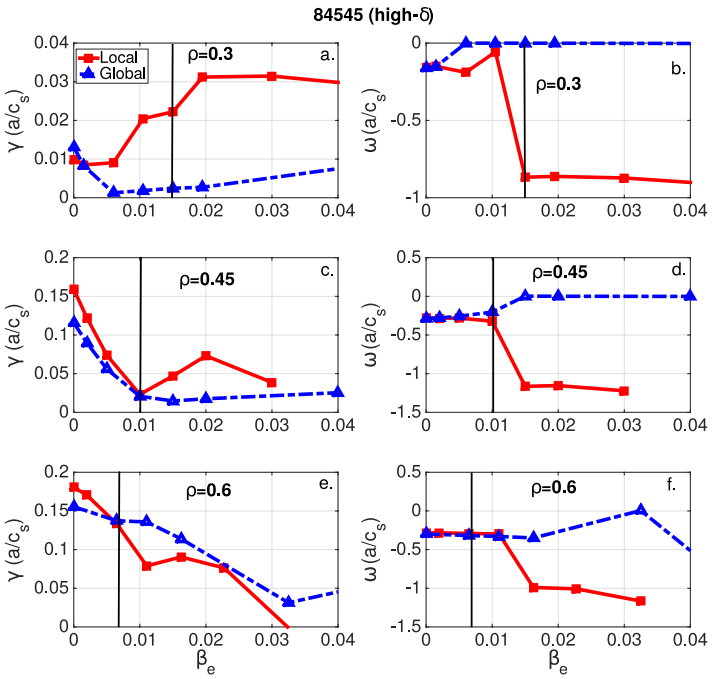

Figure 4.1 – Imaginary and real frequencies of the most unstable modes as a function of β_e with self-consistent variation of the α_{MHD} for the discharge 84545. The vertical lines represent the experimental values of β_e. [37].

Global simulations, on the other hand show a strong stabilisation of ITGs as β is increases : the growth rate remains almost null while the frequency shifts very close to zero.

Conclusions. Global results in this linear analysis are encouraging since they imply that the magnetic pressure of the plasma can be pushed higher than previously thought without degradation of confinement [37]. Discrepancies between local and global results can be attributed to profile variation effects, which obviously can't be taken into account in local simulations.

4.2.2 Role of the Shafranov shift

The delayed onset of an ITG-KBM transition can be attributed to the α_{MHD} parameter related to the Shafranov shift, which we already discussed in section 2.1.2. In GYRO, a parameter c_p exists that multiplies this α_{MHD} factor. Fig. 4.2 displays the evolution of the most unstable mode in two cases, a $c_p = 0$ case which corresponds to $\alpha_{MHD} = 0$ and a « adjusted » c_p which corresponds to a self-consistent value for α_{MHD}.

For $\rho = 0.45$ it can be seen that global and local simulations show a rather similar behaviour when Shafranov shift effects are cancelled. Indeed, global simulations now clearly show an ITG-KBM transition as well while the local picture remains mostly unchanged.

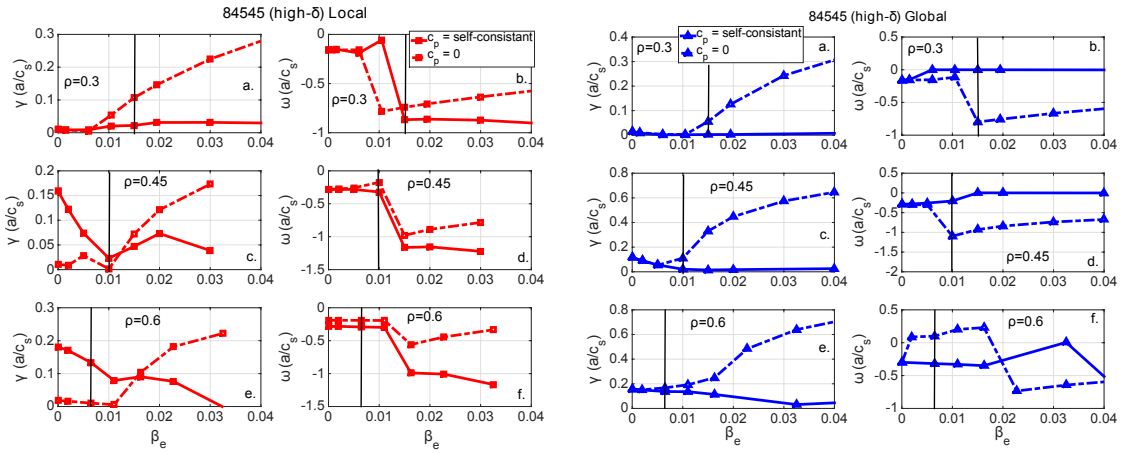

Figure 4.2 – Imaginary and real frequencies of the most unstable modes as a function of β_e with with (solid lines) and without (dashed lines) Shafranov shift effects in discharge 84545. The vertical line represents the experimental values of β_e [37].

4.2.3 Role of the magnetic shear

Shear effects were investigated by conducting simulation where magnetic shear was increased by 30%. The procedure to produce the altered profile can be found in [31]. Results are reported in fig. 4.3. In local simulations, an increased magnetic shear stabilises the plasma at all radii. In global simulations, growth rate were already very low, but we can see that the dominant mode at high β has a positive frequency between 0 and 0.5, which points at tearing electron modes (TEM).

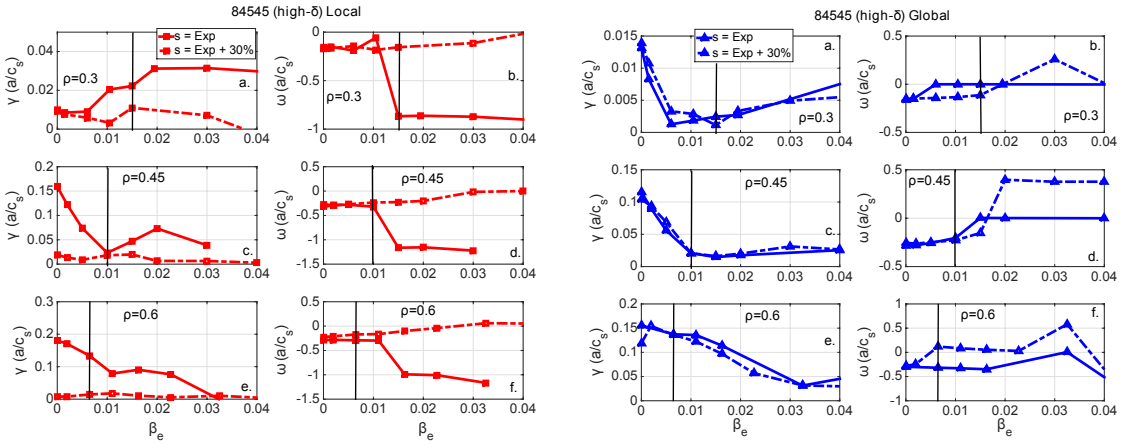

Figure 4.3 – Imaginary and real frequencies of the most unstable modes as a function of β_e with with (solid lines) and without (dashed lines) Shafranov shift effects in discharge 84545. The vertical line represents the experimental values of β_e [37].

4.3 Analysis of the non-linear results

In a non-linear study, all the modes are looked at, and simply tracing the evolution of the frequencies as we increase β isn't possible anymore. We will thus have to look directly at a certain number of « diagnostic tools » from which we will infer the behaviour of the plasma.

Four such diagnostics are used : the energy content of each mode classified per wavevector in a histogram, the potential frequency response, the fluctuations of the potential in space itself, and the evolution of the amplitude of the modes versus time. A fifth diagnostic, the evolution of particle or heat fluxes versus time, is used to determine whether or not a simulation has reached steady state.

4.3.1 Results and commentary

Heat fluxes

Normalised ionic heat fluxes for all runs are shown in fig. 4.4.

In all runs but the high-β cases, the heat flux evolution is following a very recognisable pattern : a more or less short period of flatlining, followed by a brutal increase, and later stabilising at a quasi-stationary value. The initial near-zero period lasts as long as modes aren't strong enough to have an effect. As we'll see in a moment, a basic observation of our runs indicates that, the higher the β, the more damped the modes will be (at least for the first three runs). This explains why the flatline period lasts longer and longer as β is increased. The sharp increase in flux that follows happens within the linear regime, when modes (such as ITGs) are increasing independently from each other and transporting heat from hot, dense core towards the colder, thinner edge. As a linear phenomenon, this rise is exponential. After a certain point however, saturation will take place and will stabilise the flux, which is the sign we've entered the non-linear regime.

On the other hand, the two high-β cases, namely the $\beta = 1.2\beta_{\text{exp}}$ and the $\beta = 1.5\beta_{\text{exp}}$ cases, have not reached a quasi-stationary state. This was mostly due to a lack of time, as these runs, very rich in instabilities, take very long to converge. We nevertheless believe they hold sufficient information to draw preliminary conclusions, although some caution will naturally have to be exercised. The intermediate high-β case seems very likely to converge properly if given enough time, and we are thus confident that we will eventually be able to treat it on the same footing as the others once this will be the case.

The high-β case however, is more hazardous to predict in that regard. Indeed, it has only undergone a very small amount of timesteps with the initial, linear rise being only it very early stages (the normalised ionic thermal flux has only reached value of $Q_I/Q_{GB} = 0.008$ while the peak is only expected at $Q_I/Q_{GB} \approx 10$, and it exhibits a very particular oscillating behaviour, which is believed to be due to at least two competing modes of similar strength. Because of all these elements, it is too early to tell if quasi-stability will eventually be reached here.

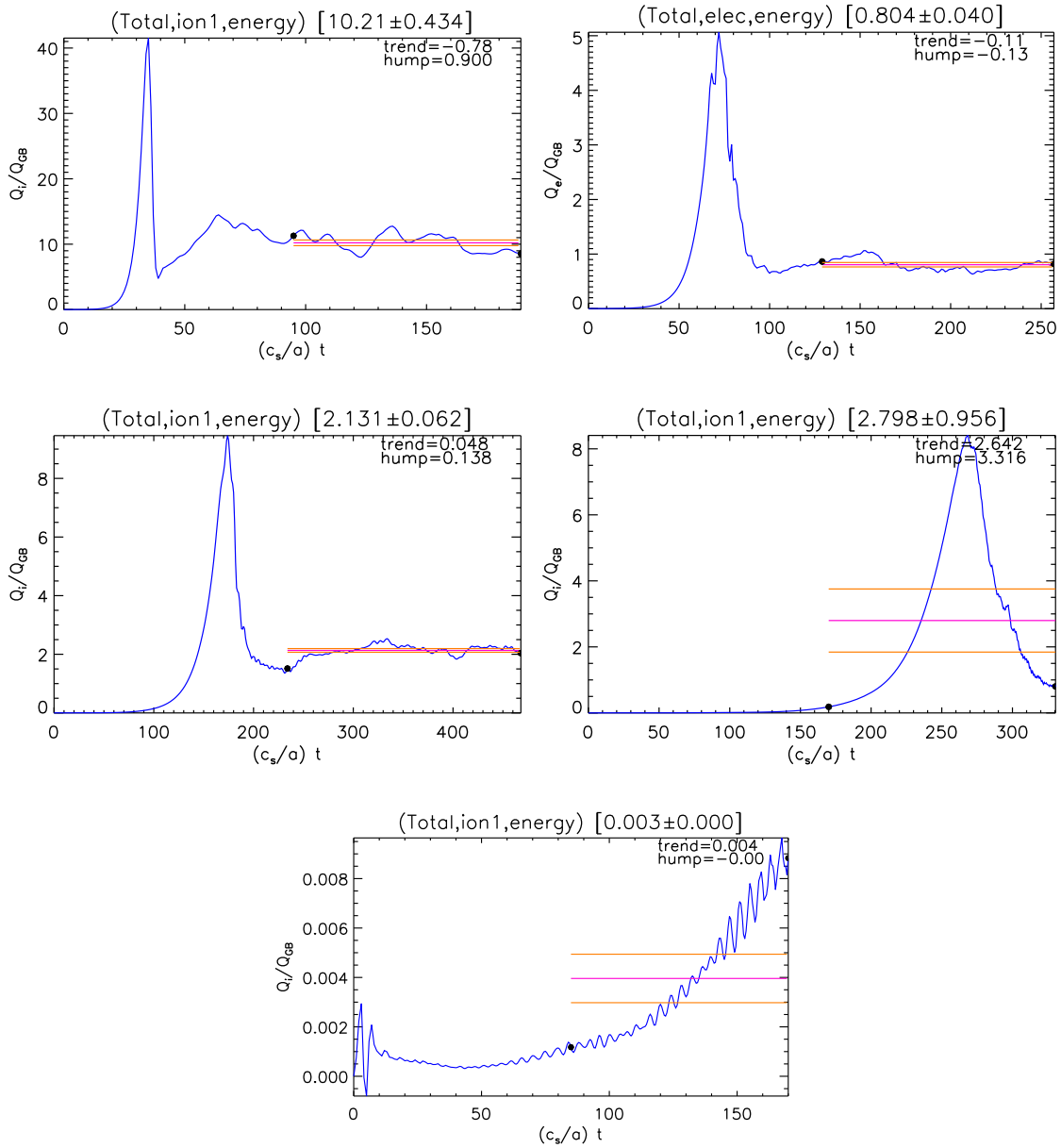

Figure 4.4 – Non-linear analysis of discharge 84545 : fluxes for all beta cases (in reading order : zero β, low β, experimental β, intermediate high β and high β).

Mode histogram and potential fluctuations

The mode histograms for all runs are shown in fig. 4.5 while the potential fluctuation spatial graphs are displayed in fig. 4.6.

As the β parameter is increased from 0 to its experimental value, a most prominent consequence is that all modes carry significantly less and less energy, as it can be seen from the y-axis of the mode histogram. We also see that the peak (indicating the group of modes that carry the most energy) at $k_\theta \rho_s = 0.35$ becomes less prominent while another one, centred $k_\theta \rho_s = 0.35$. Based on the first three runs, this new peak suggests the birth of KBMs. Note that this « stretching-out » of modes (a smaller wavevector means a larger perturbation) can also be seen directly on the potential fluctuations graph, which shows the amplitude of potential fluctuations $\delta\phi$ in physical space.

The mode histogram for the intermediate high β case does not seem, however, to indicate a strengthening of the $k_\theta \rho_s = 0.2$ mode and displays a pure ITG picture instead. This is rather unexpected, and we thus believe that it is best to carry on the run until stabilisation before drawing any conclusion. It is indeed likely that KBMs will emerge from there. The potential fluctuations graph for this run is unavailable due to time constrains.

The same remarks hold true for the high β run, which in this case displays a rich plethora of very small-scale modes, with no clear dominant mode. Some of which are electron temperature gradient modes (ETGs), although they are only visible on the potential frequency response, which is analysed in the next subsection. The potential fluctuations snapshot at $t = 170a/\bar{c}_s$ shows only large radial fluctuation, but here again, this is at a time when the solution hasn't converged yet, and can't be taken as representative of the run.

Potential frequency response

Potential frequency response graphics for all available runs can be seen on fig. 4.7.

The potential frequency response graphs seem to show that most modes have a frequency between $(a/\bar{c}_s)\omega = 0$ and -0.2, which is typical of ITGs. At zero β, the distribution is very spread out, but as it is increased, the peak becomes more evident. We also see less and less modes as the β parameter is increased, which, again points out at ITG stabilisation.

On the experimental β run graphic, we can also see a slightly brighter area located around $(a/\bar{c}_s)\omega = -1.1$ for toroidal wave numbers between 10 and 30. Modes with these kind of frequencies are typically KBMs ; we may thus be observing the onset of such modes.

The high β simulation in its current state does not allow us to clear the situation out, but several interesting observations can be made. The bulk of the instabilities are ITGs as shown by the bright zone near the centre, a feature in line with the other runs. There are also mode visible at toroidal wave numbers around 60, and more generally, modes with frequencies around $(a/\bar{c}_s)\omega = -1.45$ seem to be slightly more prominent across the toroidal spectrum, which is also hinting at KBMs. Lastly, electron-driven modes, characterised by their positive frequencies, are also visible.

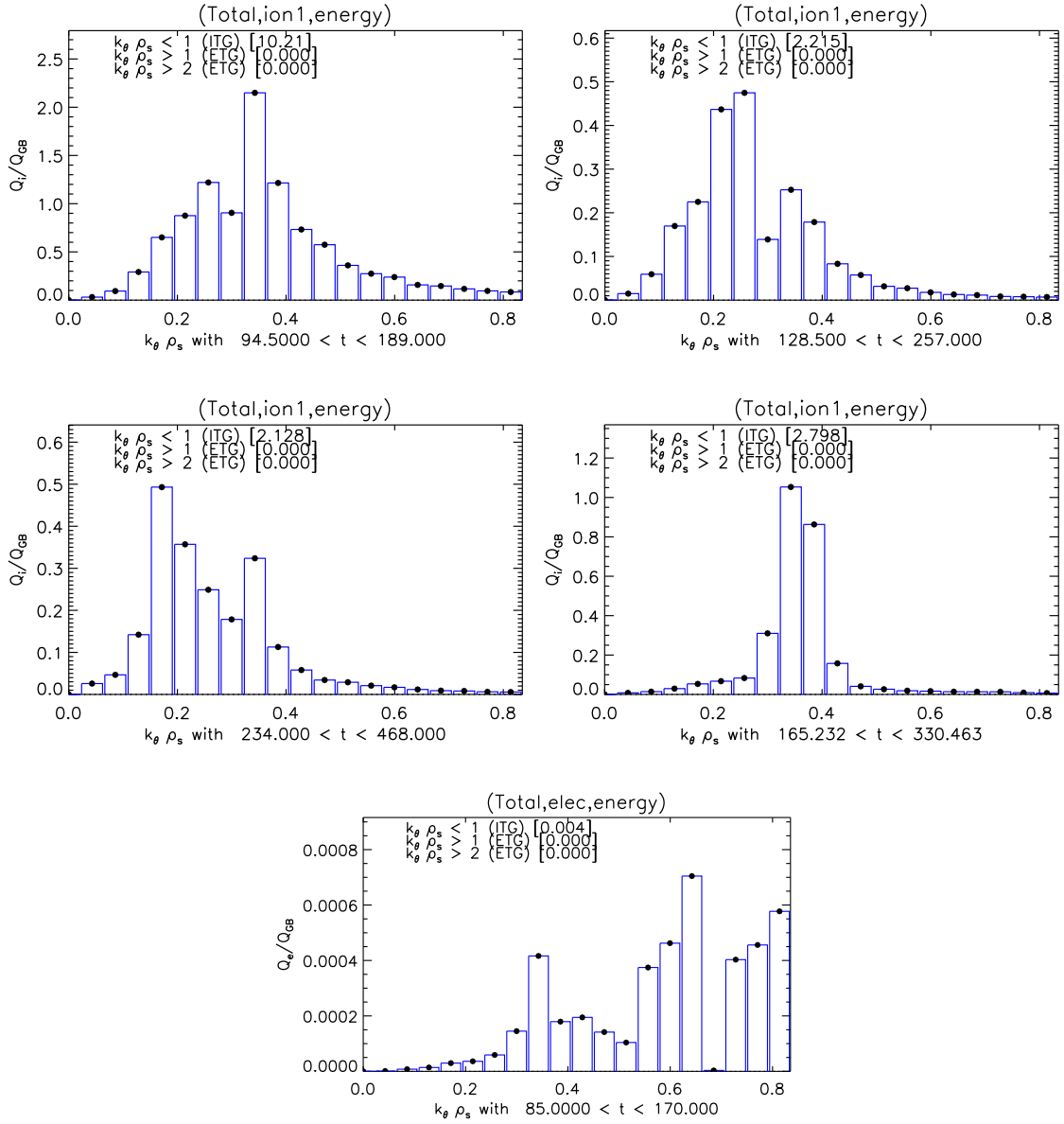

Figure 4.5 – Non-linear analysis of discharge 84545 : mode histograms for all beta cases (in reading order : zero β, low β, experimental β, intermediate high β and high β).

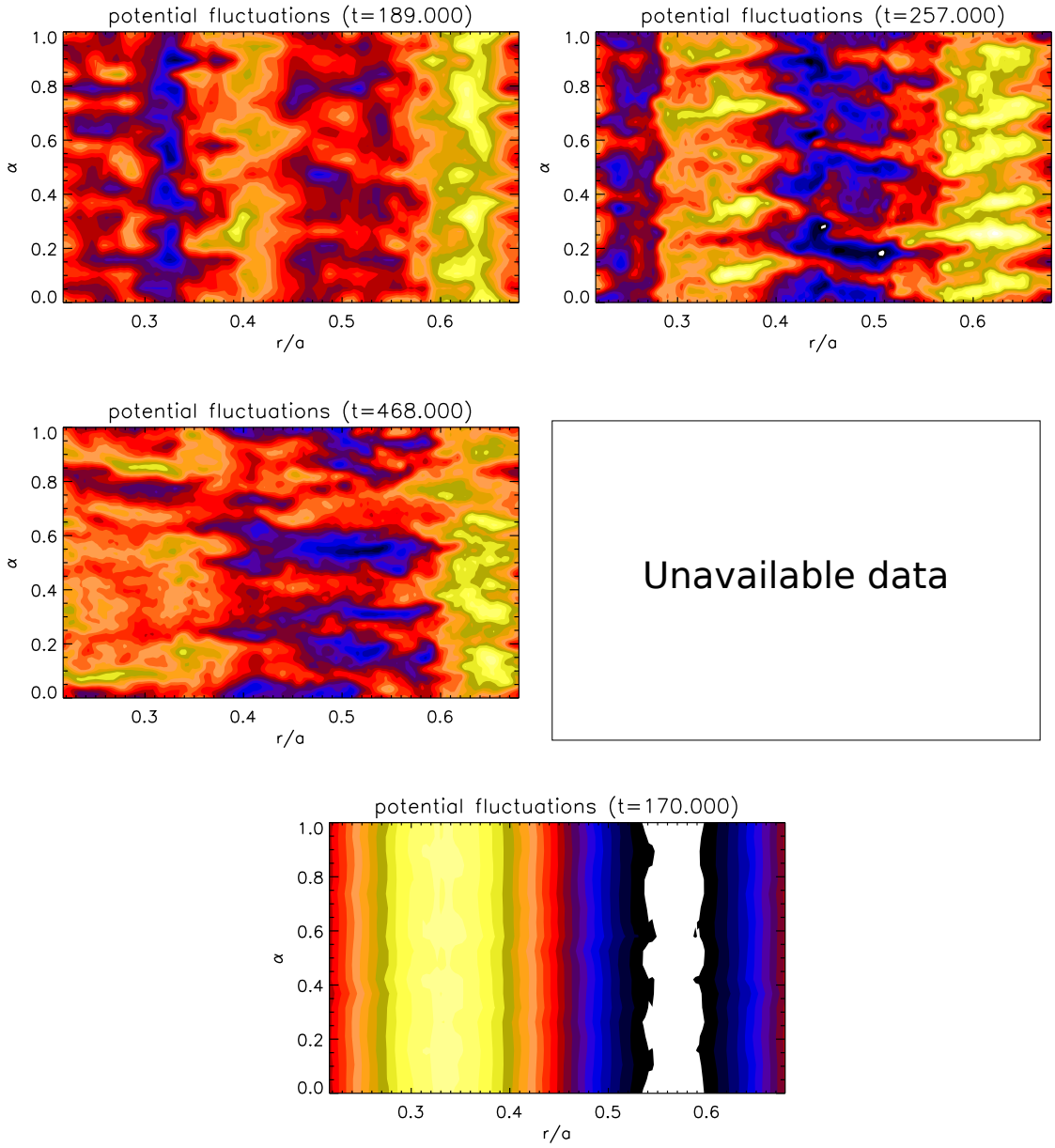

Figure 4.6 – Non-linear analysis of discharge 84545 : potential fluctuations for all beta cases (in reading order : zero β, low β, experimental β, intermediate high β and high β).

The intermediate high β plot couldn't be produced because of time constrains.

Microinstabilites and zonal flow

Time-evolution plot of electrostatic mode amplitude for all runs are displayed on fig. 4.8.

In all stabilised runs, we see that, after a certain time, the zonal flow takes over the microinstabilities. This is because, once the zonal flow is strong enough, it is able to « tear apart » the microinstabilities. The onset of this zonal flow takeover increases as β is augmented, which likely to be due to Shafranov shift effects.

In both the higher β cases, the competition between the many modes present are causing a the very strong zonal flow observed along with the oscillatory behaviour already seen in the fluxes.

4.3.2 Discussion

Comparison with the linear study

Although high-beta runs did not reach stability, we believe that they were interesting enough to be analysed. Whether or not our preliminary conclusion that we indeed see an ITG-KBM transition in the core of the tokamak as the β parameter is increase in non-linear local gyrokinetic simulations hold will depend on their outcome, although we are confident that this will be the case. This would corroborate the pictures obtained from linear, local simulations analysed in [37].

It would have been interesting to perform a study with global boundary condition to allow for a full comparison with the linear case. This was tried at the very beginning of the project, in late 2015 [(i)], however, the simulations were extremely difficult to carry on, and the idea was eventually dropped after a few months' worth or attempts, in order to focus on local simulations only. The main issue encountered with the global simulations were the fact that the initial, exponential rise in the flux was very strong, and GYRO would not be able to resolve through the peak because of its sharpness, an event which obviously leads the solver to a stop. We tried making the time resolution finer by several tiers (thus also increasing the time simulations would take to complete), but as the attempt with 5×10^{-4} gyration steps was still unsuccessful, it was deemed unrealistic to expect an even finer simulation to complete within a reasonable time frame (if even successful). Several ways to overcome these obstacles are proposed in sec. 4.3.3 below.

The situation for core microinstabilities can thus be summarised in a table as shown in fig. 4.9 below.

[(i)] A global study was actually the initial goal of this thesis.

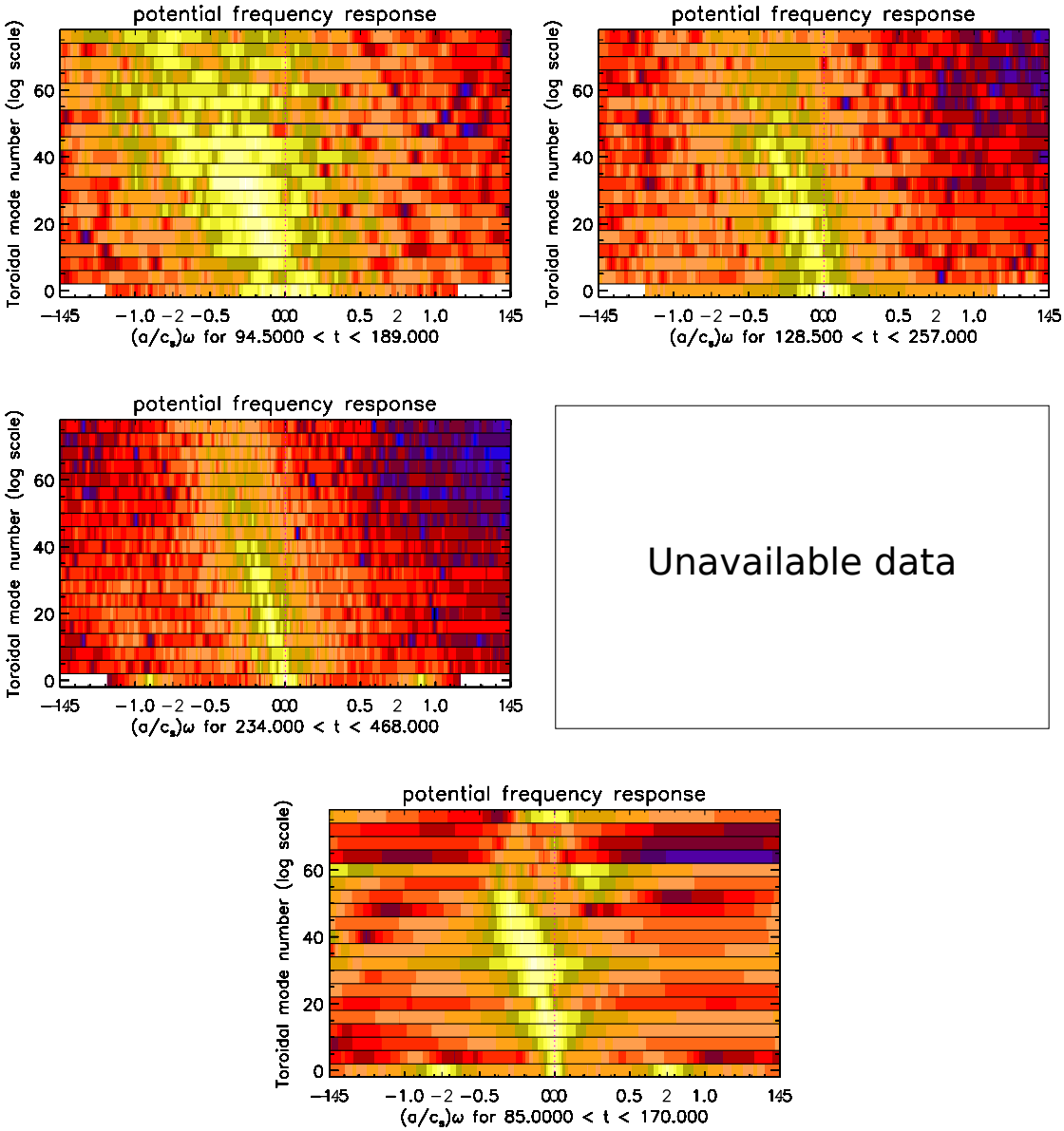

Figure 4.7 – Non-linear analysis of discharge 84545 : potential frequency response for all beta cases (in reading order : zero β, low β, experimental β, intermediate high β and high β).

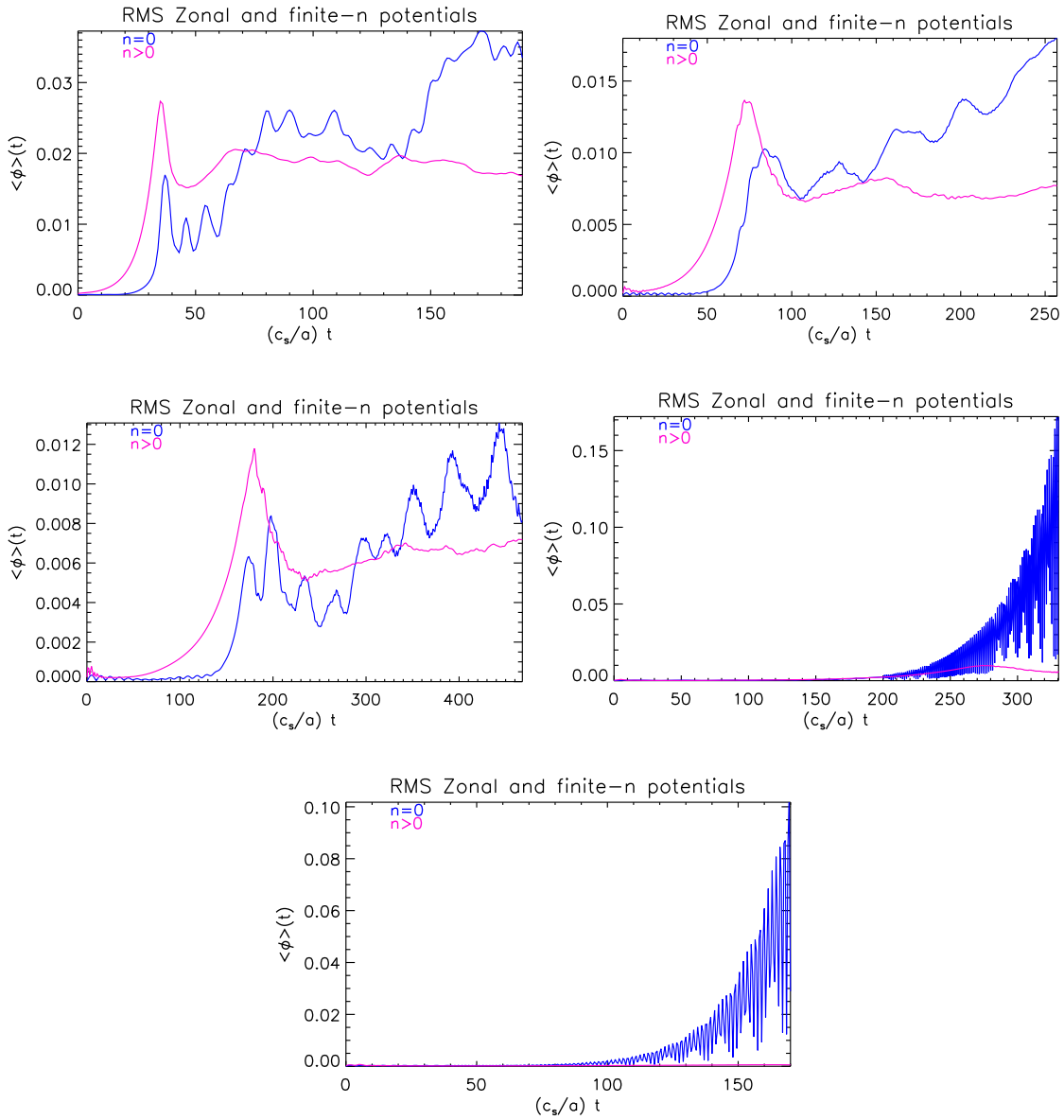

Figure 4.8 – Non-linear analysis of discharge 84545 : potential frequency response for all beta cases (in reading order : zero β, low β, experimental β, intermediate high β and high β).

	Local	Global
Linear [37]	ITG-KBM transition	Suppression of ITGs
Non-linear	**Possible ITG-KBM transition**	N.A.

Figure 4.9 – Summary of the outcomes of all the core microinstabilities studies. The result of our own simulations, a local, non-linear one is highlighted in bold text.

Feedback from the 02/02/2016 presentation at CCFE

In early February 2015, we participated to a small, internal conference at the Culham Centre for Fusion Energy (CCFE), in Oxford, UK, the organism housing, among other facilities, the JET. We recalled the results of the linear study by Moradi *et al.* [37] and presented preliminary data from our non-linear simulations. We already hinted at the possibility that the conclusions from both studies would be similar, *viz.* that ITGs become only marginally unstable in global simulations while they undergo a transition to KBM in local ones.

Among the feedback that we received, one researcher voiced concerns that our results were in disagreement with the results she previously obtained [15][46]. She suggested that ITGs shouldn't be stabilised as β is increased. Several reasons for the disagreement were discussed. The first element that was raised was the possibility that the discharge chosen here wasn't representative enough. However, two different discharges were examined in the linear study, both already well-studied within the community [8] and they were showing similar results. The discharge used here is the same as in [37]. Out of curiosity, we nevertheless tried to steepen the profiles used in our study by a factor two, as shown in fig. 4.10 but in this case the simulations were yielding unphysical results.

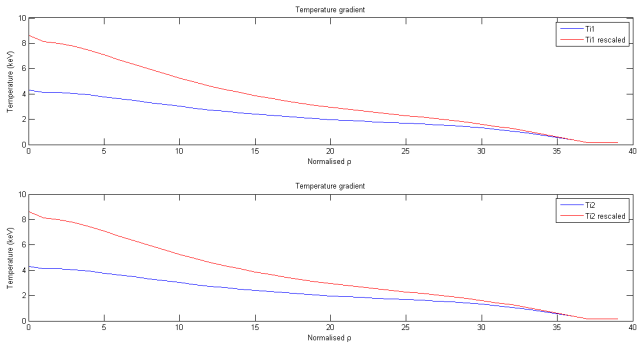

Figure 4.10 – Original and rescaled profiles. Simulations were re-run using the new profiles to see if that could contradict our hypothesis that higher βs stabilise ITGs, but we obtained non-physical results instead.

Ultimately, we believe that the discrepancy can be attributed to the use of the geometry in which the simulations have been conducted, that is, the way magnetic field and flux surfaces are modeled. While this study and the linear one were conducted with a realistic geometry that

accounts for most of the features of a tokamak [6], the model used in [15] is a much simpler one, the $s - \alpha$ model [11]. We have not yet rerun our simulations with this particular flux geometry model to check if this hypothesis for the discrepancy is indeed correct, but it would be conceivable to verify this in the near future, since GYRO supports this model as well.

4.3.3 Possible follow-on studies

The most straightforward perspective of this present study is of course to carry on the higher beta simulations until completion to verify whether or not the conclusions we hinted still hold. We are however fairly confident that this will be the case.

What our non-linear study primarily lacks at this point is a analysis with global boundary conditions. This would of course allow for a more complete and meaningful comparison with the linear study, but the results would also, in theory, be closer to reality[(ii)]

As explained earlier, we weren't able to produce results for global simulations using GYRO because the linear rise would be too strong to allow the solver to resolve an individual time step. In this section we will list several ways we envision to get past this issue.

An important limitation of GYRO in its present form is that the resolution of the simulations can't be modified in mid-way. In order to complete a simulation involving sharp increases in fluxes, we are thus forced to set a very fine resolution to resolve this particular part, even if a great portion of the simulation could be carried on at much lower resolution, thus vastly increasing the time needed to complete it. Another open-source gyrokinetic solver, GENE, developed under the leadership of F. Jenko at the IPP [28], allows for such modification of the resolution during the simulation. This would thus allow to carry on the simulation at reasonable resolution while being able to increase it only in the section that causes issues, thus most probably resulting in successful global non-linear runs. While we deemed important to continue using GYRO for our non-linear study in order to be able to meaningfully compare our results to the linear one (which also used GYRO), we are here forced to look for an alternative. Non-linear local simulations, which GYRO was able to complete, could be rerun on GENE to have a point of comparison, and if results are similar enough, the results of global non-linear simulations with GENE could be considered a valid confirmation of the linear analysis.

Another way out is to make use of the method explained in a recent paper by P. A. Abdoul *et al.* that aims to reconstruct the global eigenmode structure by combining results from local gyrokinetic simulations [1]. It would certainly be much more straightforward to use GENE to run our global non-linear simulations, and we still have to thoroughly check if the method described in [1] can really be applied in our case, but in the even of a failure by GENE to complete the desired simulations, the paper will most certainly deserve a very close look.

[(ii)] As already mentioned earlier in this thesis, global gyrokinetic simulations remain a sensitive topic within the community, partly because a number of artificial parameters have to be added in order to keep getting physically-acceptable results [6][35].

Chapter 5

Conclusions

Huge strides have been made in the field of magnetically-confined fusion since the T-3 tokamak of the Kurchatov Institute, U.S.S.R., became the first working nuclear reactor in 1968. The device was crude by modern standards and suffered important radiation losses, but for the first time, a fusion reaction could be claimed to be controlled, even if it was only for a few milliseconds [44]. Rapid development followed, notably through the investigation of more efficient heating technologies, but to reach the point of ignition, where the reaction would be self-sustaining, was still a distant prospect. Among the main hurdles, the fractional nature of our understanding of confinement mechanisms, the limited computational resources available to fully study plasma instabilities as well as the technological and industrial challenges that accompany the construction of very large vessels can be cited.

Today, the *Joint European Torus* (JET) can achieve discharges producing up to 16MW of fusion power during several seconds, and while its performances still falls short of reaching the ignition point, the next big milestone device, the *International Thermonuclear Experimental Reactor* (ITER) is predicted with great confidence to achieve that goal [12]. Thanks to the data accumulated by tokamaks of all sizes and shapes from all over the world, combined with progress in supercomputer technology, the behaviour fusing plasmas is understood better and better, and predictions of tokamak performances is becoming more and more accurate. While manufacturing processes have considerably improved as well, the technological challenges to build tokamak parts at reasonable costs remain important, and are the subject of large R&D efforts [14].

While the main issues faced by ITER at the moment are indeed industrial rather than scientific [12], plasma physics still has a capital role to play in the advent of fusion power generation. Indeed, a better understanding of confinement might lead to future reactors being smaller or demanding less power to be run than what is currently envisioned. Our current study, and more generally, the effort to understand plasma instabilities is to be seen in that framework. If the thesis supported by [37] that core ITGs are indeed marginally suppressed when the β parameter of a tokamak is increased, this might mean that future tokamak could be run with

weaker magnetic fields, which means less currents and less stresses on the vessel structure.

What we have concretely shown in this study is that, *locally, the results obtained with a non-linear analysis of core microinstabilities agree with the results obtained with a linear analysis, that is, that ITGs undergo a transition to KBMs as the β parameter is increased.* While this does not prove, of course, the findings of [37] for global simulations, this raises hope that they are confirmed as well. To run these simulations globally was the initial goal of this thesis, but due to the limitations of GYRO, we have confined ourselves to the local half of the problem. At the end of our analysis, we have nevertheless envisioned several ways to achieve this next step.

Appendices

Appendix A

Details on JET run n° 84545

This appendix regroups the time traces and profiles characterising the JET run n° 84545, which we have analysed here. The original data comes from [8] but the graphs were taken from [31].

A.1 Time traces

The time traces of our run, which are simply functions of several relevant parameters versus time, can be found in fig. A.1 below. P_{tot} represents the total power injected in the tokamak. Several heating mechanisms have been described in sec 2.1.1 ; in our case, most of the power comes from NBIs. I_{plasma} is the current flowing through the plasma. β_N is the normalised β parameter, a dimensionless quantity, defined in sec. 2.1.2. The $H_{98(y,2)}$ factor is the normalised confinement time defined at eq. 2.19. Finally, F_{GDL} is the Greenwald density fraction, which represents the average density divided by a normalisation.

A.2 Profiles

Profiles are radial functions of parameters relevant to the discharge. In fig. A.2 are regrouped the profiles pertaining to the plasma itself. The left column displays, from top to bottom, the electron density, the electron temperature, and the ion temperature, while the right column shows the derivative of these quantities with respect to the radius. Fig. A.3 on the other hand, depicts the profiles related to the magnetic field ; in reading order, the electronic β parameter discussed in sec. 2.1.2, the α_{MHD} parameter defined at eq. 2.12, the safety factor q defined at eq. 2.14, and finally the s factor, which is defined on the graph itself.

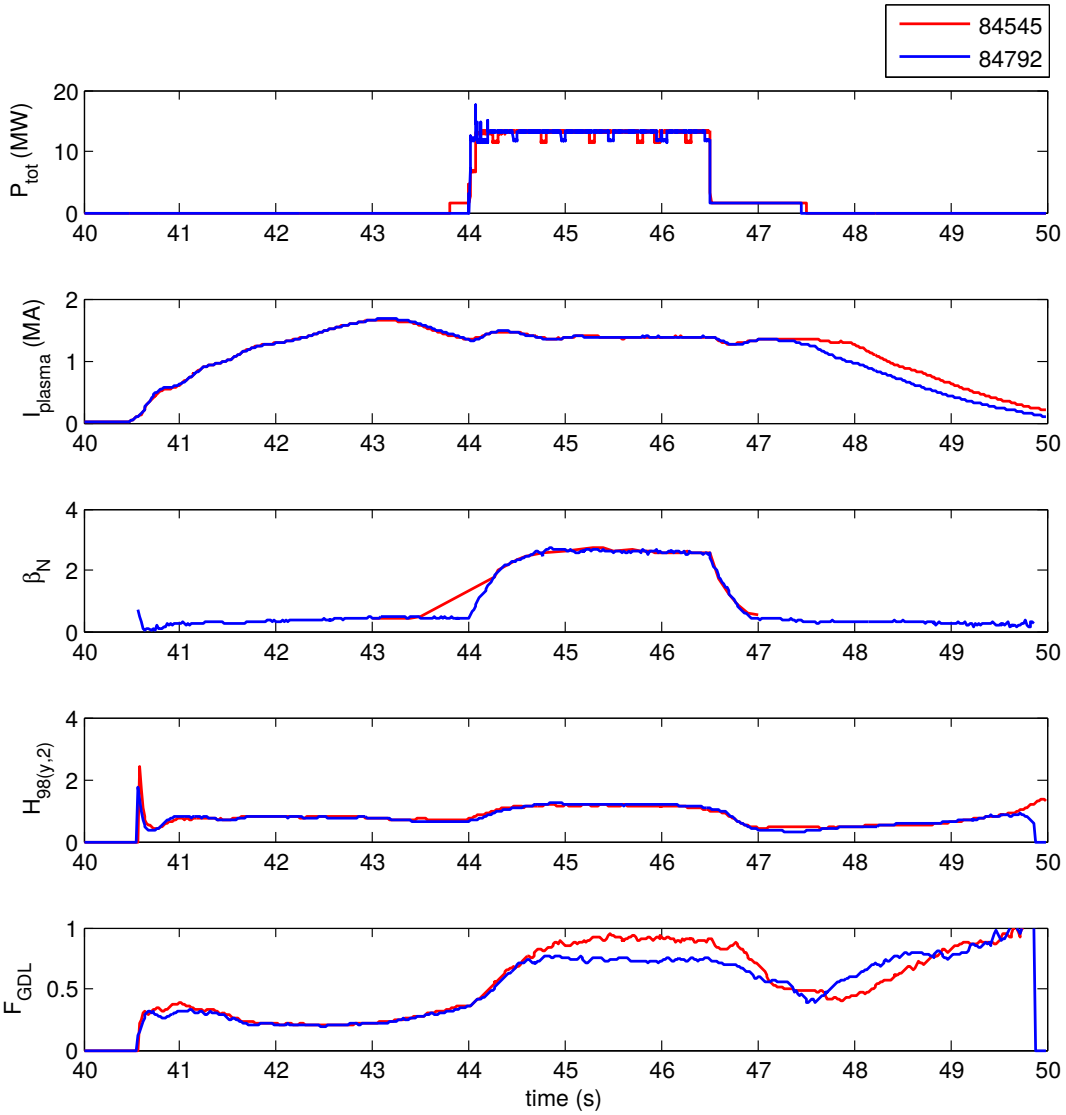

Figure A.1 – Time traces. Run n° 84545 is indicated by the red curve.

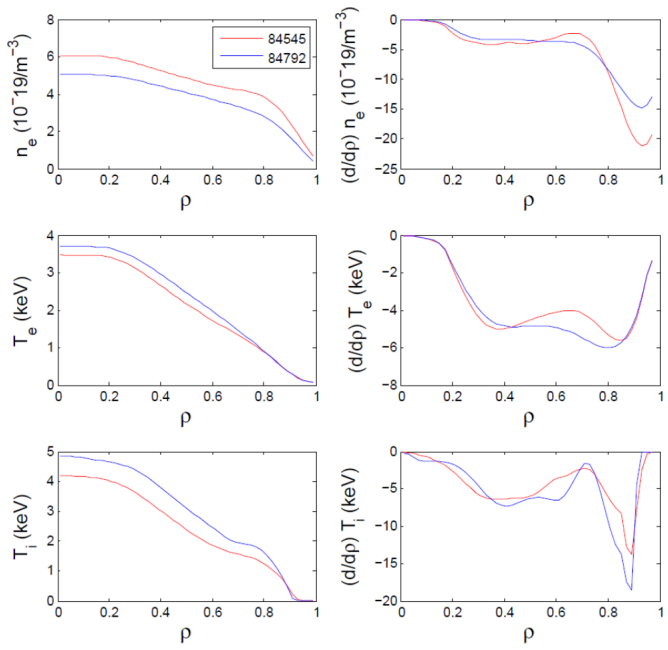

Figure A.2 – Profiles of plasma parameters. Run n° 84545 is indicated by the red curve.

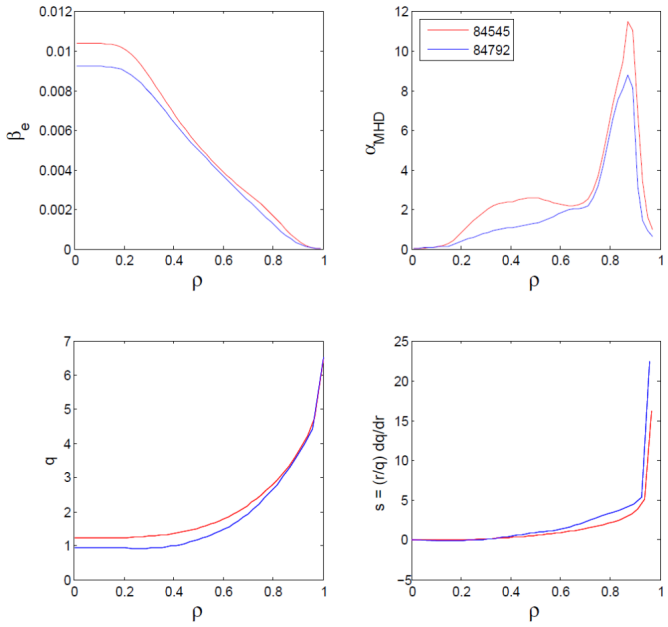

Figure A.3 – Profiles of geometric parameters. Run n° 84545 is indicated by the red curve.

Appendix B

Details on the simulation parameters

In the appendix, we are sharing the contents of the `input.gyro` file, which contains all the relevant numerical parameters of the simulations, for reproducibility. A more complete and user-friendly file `out.gyro.run` exists but would be too large to display here. It can however be directly generated from `input.gyro` and the profiles by GYRO.

B.1 Zero beta

```
#===================
#Rotation-specific parameters
GAMMA_E=0.0
PGAMMA=0.0
MACH=0.0
#===================

# Plasma shape/geometry
RADIAL_PROFILE_METHOD=3
#===================

# Plasma profiles
ELECTRON_METHOD=2
N_FIELD=1
DENSITY_METHOD=2

# deuterium
Z=1.000000
MU=1.000000

NU_EI_SCALE=1.0

# electron
MU_ELECTRON=60.000000
#===================
# Numerical resolution
TOROIDAL_GRID=20
BOX_MULTIPLIER=2
TOROIDAL_MIN=0
TOROIDAL_SEP=4

TIME_STEP=0.001
TIME_MAX=1000
TIME_SKIP=1000

# radial resolution

RADIAL_GRID=128
RADIAL_DERIVATIVE_BAND=4
RADIAL_GYRO_BAND=14

# poloidal resolution

ORBIT_GRID=8
BLEND_GRID=10

# velocity resolution

PASS_GRID=4
TRAP_GRID=4
ENERGY_GRID=8
ENERGY_MAX=6.0
#===================
```

```
                            AMP_PHI_0=1e-4
# Control parameters                                LINDIFF_METHOD=3
Z_EFF_METHOD=1              THETA_PLOT=32           #===================
BOUNDARY_METHOD=1
NONLINEAR_FLAG=1            PLOT_U_FLAG=1           RADIUS=0.45
#EXPLICIT_DAMP_GRID=8       PLOT_N_FLAG=0           GEO_BETAPRIME_SCALE=0.0
                            PLOT_E_FLAG=0           AMPERE_SCALE=0.0
AMP_PHI_N=1e-4              PLOT_V_FLAG=0
```

B.2 Low beta

```
#===================       # Numerical resolution    ENERGY_MAX=6.0
#Rotation-specific parameters TOROIDAL_GRID=20       #===================
GAMMA_E=0.0                 BOX_MULTIPLIER=2
PGAMMA=0.0                  TOROIDAL_MIN=0          # Control parameters
MACH=0.0                    TOROIDAL_SEP=4          Z_EFF_METHOD=1
#===================                                BOUNDARY_METHOD=1
                            TIME_STEP=0.001         NONLINEAR_FLAG=1
# Plasma shape/geometry     TIME_MAX=1000           #EXPLICIT_DAMP_GRID=8
RADIAL_PROFILE_METHOD=3     TIME_SKIP=1000
#===================                                AMP_PHI_N=1e-4
                            # radial resolution     AMP_PHI_0=1e-4
# Plasma profiles
ELECTRON_METHOD=2           RADIAL_GRID=128         THETA_PLOT=32
N_FIELD=2                   RADIAL_DERIVATIVE_BAND=4
DENSITY_METHOD=2            RADIAL_GYRO_BAND=14     PLOT_U_FLAG=1
                                                    PLOT_N_FLAG=0
# deuterium                 # poloidal resolution   PLOT_E_FLAG=0
Z=1.000000                                          PLOT_V_FLAG=0
MU=1.000000                 ORBIT_GRID=8
                            BLEND_GRID=10           LINDIFF_METHOD=3
NU_EI_SCALE=1.0                                     #===================
                            # velocity resolution
# electron                                          RADIUS=0.45
MU_ELECTRON=60.000000       PASS_GRID=4             GEO_BETAPRIME_SCALE=0.5
#===================       TRAP_GRID=4             AMPERE_SCALE=0.5
                            ENERGY_GRID=8
```

B.3 Experimental beta

```
#====================
#Rotation-specific parameters
GAMMA_E=0.0
PGAMMA=0.0
MACH=0.0
#====================
# Plasma shape/geometry
RADIAL_PROFILE_METHOD=3
#====================
# Plasma profiles
ELECTRON_METHOD=2
N_FIELD=2
DENSITY_METHOD=2

# deuterium
Z=1.000000
MU=1.000000

NU_EI_SCALE=1.0
# electron
MU_ELECTRON=60.000000
#====================
# Numerical resolution

TOROIDAL_GRID=20
BOX_MULTIPLIER=2
TOROIDAL_MIN=0
TOROIDAL_SEP=4

TIME_STEP=0.001
TIME_MAX=1000
TIME_SKIP=1000

# radial resolution

RADIAL_GRID=128
RADIAL_DERIVATIVE_BAND=4
RADIAL_GYRO_BAND=14

# poloidal resolution

ORBIT_GRID=8
BLEND_GRID=10

# velocity resolution

PASS_GRID=4
TRAP_GRID=4
ENERGY_GRID=8
ENERGY_MAX=6.0
#====================

# Control parameters
Z_EFF_METHOD=1
BOUNDARY_METHOD=1
NONLINEAR_FLAG=1
#EXPLICIT_DAMP_GRID=8

AMP_PHI_N=1e-4
AMP_PHI_0=1e-4

THETA_PLOT=32

PLOT_U_FLAG=1
PLOT_N_FLAG=0
PLOT_E_FLAG=0
PLOT_V_FLAG=0

LINDIFF_METHOD=3
#====================

RADIUS=0.45
GEO_BETAPRIME_SCALE=1.0
AMPERE_SCALE=1.0
```

B.4 Intermediate high beta

```
#====================
#Rotation-specific parameters
GAMMA_E=0.0
PGAMMA=0.0
MACH=0.0
#====================
# Plasma shape/geometry
RADIAL_PROFILE_METHOD=3
#====================
# Plasma profiles
ELECTRON_METHOD=2
N_FIELD=2
DENSITY_METHOD=2

# deuterium
Z=1.000000
MU=1.000000

NU_EI_SCALE=1.0
# electron
MU_ELECTRON=60.000000
#====================
# Numerical resolution
TOROIDAL_GRID=20
BOX_MULTIPLIER=2
TOROIDAL_MIN=0
TOROIDAL_SEP=4

TIME_STEP=0.00001
TIME_MAX=1000
TIME_SKIP=10
```

```
                              PASS_GRID=4
# radial resolution           TRAP_GRID=4                 THETA_PLOT=32
                              ENERGY_GRID=8
RADIAL_GRID=128               ENERGY_MAX=6.0              PLOT_U_FLAG=1
RADIAL_DERIVATIVE_BAND=4      #===================       PLOT_N_FLAG=0
RADIAL_GYRO_BAND=14                                       PLOT_E_FLAG=0
                              # Control parameters        PLOT_V_FLAG=0
# poloidal resolution         Z_EFF_METHOD=1
                              BOUNDARY_METHOD=1           LINDIFF_METHOD=3
ORBIT_GRID=8                  NONLINEAR_FLAG=1            #===================
BLEND_GRID=10                 #EXPLICIT_DAMP_GRID=8
                                                          RADIUS=0.45
# velocity resolution         AMP_PHI_N=1e-4              GEO_BETAPRIME_SCALE=1.2
                              AMP_PHI_0=1e-4              AMPERE_SCALE=1.2
```

B.5 High beta

```
#===================          TOROIDAL_GRID=20            #===================
#Rotation-specific parameters BOX_MULTIPLIER=2
GAMMA_E=0.0                   TOROIDAL_MIN=0              # Control parameters
PGAMMA=0.0                    TOROIDAL_SEP=4              Z_EFF_METHOD=1
MACH=0.0                                                  BOUNDARY_METHOD=1
                              TIME_STEP=0.0005            NONLINEAR_FLAG=1
#===================          TIME_MAX=1000               #EXPLICIT_DAMP_GRID=8
# Plasma shape/geometry       TIME_SKIP=2000
RADIAL_PROFILE_METHOD=3                                   AMP_PHI_N=1e-4
                              # radial resolution         AMP_PHI_0=1e-4
#===================
# Plasma profiles             RADIAL_GRID=128             THETA_PLOT=32
ELECTRON_METHOD=2             RADIAL_DERIVATIVE_BAND=4
N_FIELD=2                     RADIAL_GYRO_BAND=14         PLOT_U_FLAG=1
DENSITY_METHOD=2                                          PLOT_N_FLAG=0
                              # poloidal resolution       PLOT_E_FLAG=0
# deuterium                                               PLOT_V_FLAG=0
Z=1.000000                    ORBIT_GRID=8
MU=1.000000                   BLEND_GRID=10               LINDIFF_METHOD=3
                                                          #===================
NU_EI_SCALE=1.0               # velocity resolution
                                                          RADIUS=0.45
# electron                    PASS_GRID=4                 GEO_BETAPRIME_SCALE=1.5
MU_ELECTRON=60.000000         TRAP_GRID=4                 AMPERE_SCALE=1.5
#===================          ENERGY_GRID=8
# Numerical resolution        ENERGY_MAX=6.0
```

Bibliography

[1] P. A. Abdoul, D. Dickinson, C. M. Roach, and H. R. Wilson, *Using a local gyrokinetic code to study global ion temperature gradient modes in tokamaks*, Plasma Physics and Controlled Fusion, 57 (2015), p. 065004.

[2] C. Angioni et al., *Tungsten transport in JET H-mode plasmas in hybrid scenario, experimental observations and modelling*, Nuclear Fusion, 54 (2014), p. 083028.

[3] R. Balescu, *Aspects of Anomalous Transport in Plasmas*, Series in plasma physics, IOP Publishing, 2005.

[4] M. A. Beer, *Gyrofluid models of turbulent transport in tokamaks*, PhD thesis, Priceton University, 1995.

[5] J. Candy and E. Belli, *General Atomics Report*, GA-A26818, (2011).

[6] ——, *GYRO technical guide*, (2015). `https://github.com/gafusion/doc/raw/master/gyro/gyro_technical_manual.pdf`.

[7] ——, *GYRO Overview*, Accessed : 11/01/2016. `https://fusion.gat.com/theory/Gyrooverview`.

[8] C. Challis et al., *Proceedings 25th IAEA Fusion Energy Conference*, St. Petersburg, Russia, 2014.

[9] Commisariat à l'Énergie Atomique (CEA), *A short history of magnetic fusion*, Accessed : 03/11/2015. `http://www-fusion-magnetique.cea.fr/gb/fusion/histoire/site_historique.htm`.

[10] ——, *Modes of confinement*, Accessed : 24/11/2015. `http://www-fusion-magnetique.cea.fr/gb/fusion/physique/modesconfinement.htm`.

[11] J. Connor, R. Hastie, and J. Taylor, *Shear, periodicity, and plasma ballooning modes*, Phys. Rev. Lett.; (United States), 40:6 (1978).

[12] E. Doyle et al., *Chapter 2 : Plasma confinement and transport*, Nuclear Fusion, 47 (2007), p. S18.

[13] EUROfusion, *Glossary*, Accessed : 22/11/2015. https://www.euro-fusion.org/glossary.

[14] European Fusion Development Agreement (EFDA), *Fusion electricity: A roadmap to the realisation of fusion energy*, November 2012. https://www.euro-fusion.org/wpcms/wp-content/uploads/2013/01/JG12.356-web.pdf.

[15] G. L. Falchetto, J. Vaclavik, and L. Villard, *Global-gyrokinetic study of finite beta effects on linear microinstabilities*, Physics of Plasmas, 10 (2003).

[16] R. Gabrielli and G. Herdrich, *Review of nuclear thermal propulsion systems*, Progress in Aerospace Sciences, 79 (2015), pp. 92 – 113.

[17] R. Gabrielli, D. Petkow, G. Herdrich, R. Laufer, and H.-P. Röser, *Two generic concepts for space propulsion based on thermal nuclear fusion*, Acta Astronautica, 101 (2014), pp. 129 – 137.

[18] P. Gaspard, *Physique statistique II.* Course at the Université Libre de Bruxelles, 2014.

[19] R. Goldston, *Energy confinement scaling in tokamaks: some implications of recent experiments with ohmic and strong auxiliary heating*, Plasma Phys. Control. Fusion, 26 (1984).

[20] C. Gormezano et al., *Hybrid advanced scenarios: perspectives for iter and new experiments with dominant rf heating*, Plasma Physics and Controlled Fusion, 46 (2004), p. B435.

[21] J. Graves, *Advanced theory of plasma.* Course at the École Polytechnique Fédérale de Lausanne, 2011.

[22] T. Hender et al., *Chapter 3: MHD stability, operational limits and disruptions*, Nuclear Fusion, 47 (2007), p. S128.

[23] T. C. Hender et al., *Magneto-hydro-dynamic limits in spherical tokamaks*, Physics of Plasmas, 6 (1999).

[24] O. A. Hurricane et al., *Fuel gain exceeding unity in an inertially confined fusion implosion*, Nature, 506 (20 February 2014), p. 343–348.

[25] International Atomic Energy Agency (IAEA), *Fusion: Energy of the Future*, Accessed : 10/11/2015. https://www.iaea.org/newscenter/news/fusion-energy-future.

[26] International Thermonuclear Experimental Reactor (ITER), *Fueling the fusion reaction*, Accessed : 10/11/2015. http://www.iter.org/sci/fusionfuels.

[27] F. Jenko, *Introduction to gyrokinetics*, Winter school at Les Houches, France, 2011. http://www.ens-lyon.fr/PHYSIQUE/Equipe2/LesHouches11/Talks_files/Jenko_Houches2011.pdf.

[28] F. Jenko and W. Dorland, *Nonlinear electromagnetic gyrokinetic simulations of tokamak plasmas*, Plasma Physics and Controlled Fusion, 43 (2001), p. A141.

[29] J. Johnson, *The stellarator approach to toroidal plasma confinement*, Fusion Science and Technology, 2 (1982), pp. 340–361.

[30] A. Jorissen, *Astrophysique*. Course at the Université Libre de Bruxelles, 2014.

[31] W.-J. Kettlewell, *Global vs. local gyrokinetic study of core microinstabilities in JET hybrid discharges with ITER-like wall*, (2014-2015). Master's thesis, Université Libre de Bruxelles.

[32] H. R. Koslowski, *Operational Limits in Tokamaks*, 531. WE Heraeus-Seminar, Bad Honnef, Germany, 2013. `http://www.iek-yig.de/531stWEH/talks/I5_2_Koslowski.pdf`.

[33] L. Landau and E. Lifshitz, *The Classical Theory of fields*, Course of theoretical physics, Academy of Sciences of the U.S.S.R. / Butterworth Heinemann, 4th ed., 1987.

[34] Max-Planck-Institüt für Plasmaphysik (IPP), *Stellarator*, Accessed : 29/11/2015. `http://www.ipp.mpg.de/14779/stellarator`.

[35] S. Moradi, *Private communication*, 2015.

[36] S. Moradi et al., *Core micro-instability analysis of jet hybrid and baseline discharges with carbon wall*, Nuclear Fusion, 54 (2014), p. 123016.

[37] ——, *EPS conference*, Lisbon, Portugal, 2015.

[38] A. Peeters, *Physics of fusion power, lecture 4: Cylindrical concepts*. Course at the University of Warwick, 2014.

[39] M. J. Püschel, *Electromagnetic Effects in Gyrokinetic SImulations of Plasma Turbulence*, PhD thesis, Universität Münster, 2009.

[40] M. Shimada et al., *Chapter 1 : Overview and summary*, Nuclear Fusion, 47 (2007), p. S1.

[41] J. T. Slough, *Propagating Magnetic Wave Plasma Accelerator (PMWAC) for Deep Space Exploration*, MSNW LCC and NASA Institute for Advanced Concepts, (2000).

[42] P. B. Snyder, *Gyrofluid Theory and Simulation of Electromagnetic Turbulence and Transport in Tokamak Plasmas*, PhD thesis, Priceton University, 1999.

[43] L. C. Steinhauer, *Review of field-reversed configurations*, Physics of Plasmas, 18 (2011).

[44] V. S. Strelkov, *History of the t-10 tokamak: Creation and development*, Plasma Physics Reports, 27 (2001), pp. 819–824.

[45] F. Troyon, R. Gruber, H. Saurenmann, S. Semenzato, and S. Succi, *MHD-Limits to Plasma Confinement*, Plasma Physics and Controlled Fusion, 26 (1984), p. 209.

[46] L. Villard, S. Allfrey, A. Bottino, M. Brunetti, G. Falchetto, V. Grandgirard, R. Hatzky, J. Nührenberg, A. Peeters, O. Sauter, S. Sorge, and J. Vaclavik, *Full radius linear and nonlinear gyrokinetic simulations for tokamaks and stellarators: zonal flows, applied e x b flows, trapped electrons and finite beta*, Nuclear Fusion, 44 (2004), p. 172.

[47] F. Wagner et al., *Regime of improved confinement and high beta in neutral-beam-heated divertor discharges of the asdex tokamak*, Phys. Rev. Lett., 49 (1982), pp. 1408–1412.

[48] J. Wesson, *The science of JET*. JET-R(99)13, 1999. `http://www.euro-fusionscipub.org/wp-content/uploads/2014/11/JETR99013.pdf`.

[49] J. Wesson, *Tokamaks*, Oxford University Press, 3rd ed., 2004.

[50] D. P. Whitmire, *Relativistic spaceflight and the catalytic nuclear ramjet*, Acta Astronautica, 2 (1975), pp. 497 – 509.

[51] Wikimedia. Image courtesy of Max-Planck-Institüt für Plasmaphysik (IPP) `https://commons.wikimedia.org/wiki/File:Tokamak_(scheme).jpg`.